ISSN: 1857 - 839X
DOI: 10.55302/SJCE25141

Volume 14
Issue 1
July 2025

SJCE
SCIENTIFIC JOURNAL OF CIVIL ENGINEERING

SS CYRIL AND METHODIUS UNIVERSITY
FACULTY OF CIVIL ENGINEERING

EDITORIAL - Preface to Volume 13 Issue 2 of the Scientific Journal of Civil Engineering (SJCE)

Vladimir Vitanov EDITOR - IN - CHIEF

Dear Readers,

The Scientific Journal of Civil Engineering (SJCE) is an international, peer-reviewed, open-access journal first published in December 2012 and currently issued twice a year. Since December 2021, the journal has operated entirely on a digital platform that integrates submission, review, and publication processes. More information on the digital edition is available at sjce.gf.ukim.edu.mk.

SJCE is dedicated to the dissemination of high-quality and innovative scientific research across the broad spectrum of engineering sciences. Its primary mission is to advance technical knowledge and promote pioneering engineering solutions in fields such as civil engineering, geotechnics, surveying and geospatial engineering, environmental protection, construction management, and other related disciplines. Through its open-access model, the journal ensures transparent and unrestricted access to original research papers, providing a platform for studies that address both theoretical and practical aspects of civil engineering and its associated domains.

All published papers in SJCE are assigned Digital Object Identifiers (DOI) and are distributed under the terms of the Creative Commons Attribution-ShareAlike 4.0 International License (CC BY-SA 4.0), ensuring free and open sharing of knowledge while requiring proper attribution and permitting derivative works under the same license.

As Editor-in-Chief, it is my privilege to present the first issue of Volume 14, which includes six carefully peer-reviewed research articles.

The first manuscript addresses design and dimensioning of urban street cross-sections, using Boulevard “St. Clement of Ohrid” in Skopje as a case study, with focus on balancing traffic capacity and multimodal mobility.

In the second manuscript, Author investigates the buckling behaviour of functionally graded porous plates with parabolic variable thickness resting on Pasternak foundations.

In the third manuscript, Author presents a numerical implementation of the Modified Cam-Clay (MCC) soil plasticity model using the Invariants of Stress Tensor framework to enhance geomechanics education.

In the fourth manuscript, Authors investigate the potential use of marble quarry waste from the Gjurovo locality near Prilep as a sustainable construction material.

In the fifth manuscripts, Authors examine the evolving understanding of soil shearing resistance and its implications for calculating earth pressures and designing retaining walls. In line with the National Annex to Eurocode 7 (EC7), which considers only active earth pressure, the study compares linear and non-linear interpretations of the soil failure envelope.

In the final – sixth manuscript of the current issue, Authors address the challenge of improving the sustainability of concrete structures by exploring the self-healing capability of concrete as a means to extend structural lifespan and reduce environmental impact.

In closing, I wish to express my sincere gratitude to all contributors, reviewers, and readers for their valuable engagement and support in the preparation of this issue.

Sincerely,

Vladimir Vitanov, Editor-in-Chief

July 2025

SJCE
SCIENTIFIC JOURNAL OF CIVIL ENGINEERING

Impressum

FOUNDER AND PUBLISHER

Faculty of Civil Engineering
Partizanski odredi 24, 1000 Skopje, N. Macedonia

PRINT

This Journal is printed in Mar-saz DOOEL Skopje

EDITORIAL OFFICE

Faculty of Civil Engineering
Partizanski odredi 24, 1000 Skopje, N. Macedonia
tel. +389 2 3116 066
fax. +389 2 3118 834
prodekan.nauka@gf.ukim.edu.mk

EDITOR IN CHIEF

Prof. PhD **Vladimir Vitanov**

Ss. Cyril and Methodius University in Skopje
Faculty of Civil Engineering
Partizanski odredi 24, 1000 Skopje, N. Macedonia
v.vitanov@gf.ukim.edu.mk

EDITORIAL ADVISORY BOARD

Valentina Zhileska Panchovska, PhD

Professor, Ss. Cyril and Methodius University in Skopje, Faculty of Civil Engineering, Skopje, N. Macedonia

Denis Popovski, PhD

Professor, Ss. Cyril and Methodius University in Skopje, Faculty of Civil Engineering, Skopje, N. Macedonia

Igor Peshevski, PhD

Professor, Ss. Cyril and Methodius University in Skopje, Faculty of Civil Engineering, Skopje, N. Macedonia

ISSN: 1857-839X
DOI: https://doi.org/10.55302/SJCE25141

TECHNICAL EDITORS

MSc Natasha Malijanska Andreevska

Assistant, Ss. Cyril and Methodius University in Skopje, Faculty of Civil Engineering, Skopje, N. Macedonia

MSc **Ivona Nedevska Trajkova**

Assistant, Ss. Cyril and Methodius University in Skopje, Faculty of Civil Engineering, Skopje, N. Macedonia

MSc Frosina Panovska Georgievska

Assistant, Ss. Cyril and Methodius University in Skopje, Faculty of Civil Engineering, Skopje, N. Macedonia

EDITORIAL BOARD

Marijana Lazarevska, PhD

Ss. Cyril and Methodius University in Skopje, Faculty of Civil Engineering, Skopje, N. Macedonia

Elena Dumova Jovanoska, PhD
Ss. Cyril and Methodius University in Skopje, Faculty of Civil Engineering, Skopje, N. Macedonia

Zlatko Bogdanovski, PhD

Ss. Cyril and Methodius University in Skopje, Faculty of Civil Engineering, Skopje, N. Macedonia

Ljupco Dimitrievski, PhD

Ss. Cyril and Methodius University in Skopje, Faculty of Civil Engineering, Skopje, N. Macedonia

Zlatko Zafirovski, PhD
Ss. Cyril and Methodius University in Skopje, Faculty of Civil Engineering, Skopje, N. Macedonia

Katerina Donevska, PhD

Ss. Cyril and Methodius University in Skopje, Faculty of Civil Engineering, Skopje, N. Macedonia

Tina Dasic, PhD

University of Belgrade, Faculty of Civil Engineering, Belgrade, R. Serbia

Vlastimir Radonjanin, PhD

University of Novi Sad, Faculty of Technical Sciences, Novi Sad, R. Serbia

Nenad Ivanisevic, PhD

University of Belgrade, Faculty of Civil Engineering, Belgrade, R. Serbia

Milos Knezevic, PhD
University of Montenegro, Faculty of Civil Engineering, Podgorica, Montenegro

Marina Rakocevic, PhD
University of Montenegro, Faculty of Civil Engineering, Podgorica, Montenegro

Stjepan Lakusic, PhD
University of Zagreb, Faculty of Civil Engineering, Zagreb, Croatia

Andrej Kryzanowski, PhD
University of Ljubljana, Faculty of Civil and Geodetic Engineering, Ljubljana, Slovenia

Ales Znidaric, PhD
ZAG – Slovenian National Building and Civil Engineering Institute, Ljubljana, Slovenia

Heinz Brandl, PhD
Vienna University of Technology, Institute for Geotechnics, Vienna, Austria

Resat Ulusay, PhD
Hacettepe University, Faculty of Engineering, Ankara, Turkey

SJCE
SCIENTIFIC JOURNAL OF CIVIL ENGINEERING

Impressum

ORDERING INFO

SJCE is published bi-annually. All articles published in the journal have been reviewed.

Edition: 100 copies

SUBSCRIPTIONS

Price of a single copy:
for Macedonia (500 den);
for abroad (10 EUR + shipping cost).

BANKING DETAILS (NORTH MACEDONIA)

Narodna banka na RNM
Account number:
160010421978815,
Prihodno konto 723219,
Programa 41

BANKING ETAILS (INTERNATIONAL)

Correspond bank details:
Deutsche Bundesbank
Zentrale Address: Wilhelm Epstein Strasse 14 Frankfurt am Main, Germany SWIFT BIC: MARK DE FF
Bank details:
National Bank of the RNM
Address: Kompleks banki bb 1000 Skopje, North Macedonia
SWIFT BIC: NBRM MK 2X
IBAN: MK 07 1007 0100 0036 254
Name: Gradezen Fakultet, Skopje

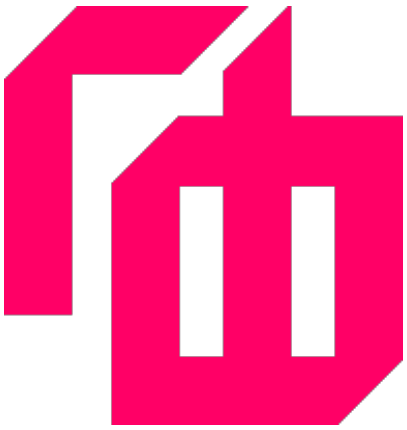

СЕКОГАШ БИДИ ИН

SJCE
SCIENTIFIC JOURNAL OF CIVIL ENGINEERING

CONTENTS

6-ти Конгрес за брани

6th Congress on Dams

16-18.10.2025

www.macold.org.mk

ЗМКГБ MACOLD

Здружение Македонски комитет за големи брани
Macedonian Committee on Large Dams

член на
member of

Меѓународна комисија за големи брани
International Commission on Large Dams

CIGB ICOLD

Kristina Ickovska
MSc in Civil Engineering
Ss. Cyril and Methodius University in Skopje
Faculty of Civil Engineering
N. Macedonia
ickovska@outlook.com

Slobodan Ognjenovic
PhD, Professor
Ss. Cyril and Methodius University in Skopje
Faculty of Civil Engineering
N. Macedonia
0000-0002-4242-9169

DESIGNING THE CROSS-SECTION OF URBAN STREETS FROM THE PRIMARY URBAN NETWORK: BOULEVARD "ST. CLEMENT OF OHRID" – SKOPJE

DOI: doi.org/10.55302/SJCE2514107i

This study analyzes the dimensioning of the cross-section profile of urban streets within the primary street network, using the example of Boulevard "St. Clement of Ohrid" in Skopje as a case study. It emphasizes that the basis for determining the cross-section is the comparison between the expected traffic load and the permitted traffic flow per lane. The number and width of lanes must be adapted not only for motor vehicles but also for public transport, cyclists, and pedestrians, ensuring safe and efficient movement for all users.

A major concern addressed is that street cross-sections are frequently designed mainly to accommodate motor vehicles, with remaining space only minimally allocated to pedestrians and cyclists. This practice overlooks the wider urban context and can negatively impact the overall quality of urban life. This study emphasizes the importance of adopting a holistic design approach that promotes non-motorized transportation and public transit to foster safer and more livable city environments.

Keywords: traffic lanes, safety, urban mobility, cyclists, pedestrians

1. INTRODUCTION

The basis for dimensioning the cross-section of a urban streets lies in comparing the design traffic load with the permissible traffic flow per traffic lane, i.e., the number of driving lanes is calculated as $n=Q_m/Q_i$. Attention must be paid to the traffic conditions (continuous or interrupted traffic flow), as the allowable traffic load per lane significantly varies depending on these conditions. Besides defining the number of lanes for motor vehicles, it is crucial to recognize that the cross-section includes other modes of transport that require a similar approach. Therefore, evaluating the capacity and level of service is a necessary process for public transport vehicles, cyclists, and pedestrians.

In reality, cross-sections are often dimensioned primarily for motor traffic, while the remaining space is distributed to pedestrian and bicycle traffic, as well as to central and lateral safety zones. Traffic issues must be addressed with a comprehensive approach based on the rational use of private motor vehicles while simultaneously promoting non-motorized transport and public transport. Otherwise, the uncontrolled and excessive use of private vehicles will completely devalue the essence of urban life and destroy space intended for people.

In the Dutch Road Safety Manual (CROW), streets that exhibit a mismatch between their function and designed geometric characteristics are called “grey streets” (grey roads). For example, a collector street intended to balance traffic flow and speed with the safety of all users and access to surrounding facilities, but designed with geometric and cross-section elements typical of an urban arterial street. This creates significant tension between the traffic function and all surrounding urban elements. To balance the designed elements with the function of the street, adjusting its cross-section is often the only viable option.

2. FUNCTIONAL ELEMENTS OF THE CROSS-SECTION

The cross-section represents the initial projection of the street through which the basic programmatic requirements are defined and the first physical contours of the future traffic space are shaped. It consists of a collection of various functional and structural elements. Their number, dimensions, and interrelationships depend on the functional classification of the street, the user structure, and the operational indicators.

Urban planners and designers must carefully adapt the widths of the cross-section elements to ensure that everything aligns with urban planning conditions, the specific types of urban traffic, and the spatial and environmental needs.

2.1 TRAFFIC LANES

The width of traffic lanes depends on the design speed, while their number is determined by the relevant traffic load and the level of service. The minimum width of a traffic lane is directly related to the width of the vehicle (maximum 2.50 m) and the lateral safety distance between vehicles. To ensure fast and safe passing of vehicles, there must be a protective distance between the vehicles themselves and between the edge of the roadway and the vehicle.

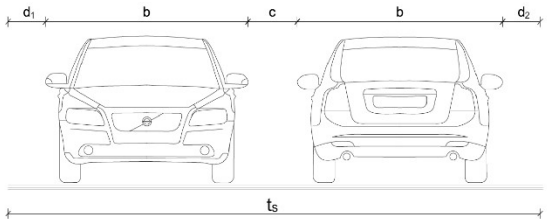

Figure 1. Carriageway width

Table 1. Traffic lane width

Design Speed V [km/h]	Lane width b [m]	2 × b = 2 × 2.50	
		c [m]	d [m]
≥ 100	**3.75**	1.70	0.40
80 ≤ V < 100	**3.50**	1.30	0.35
60 < V < 80	**3.25**	1.00	0.25
40 < V ≤ 60	**3.00**	0.80	0.10
Vr ≤ 40	**2.75**	0.30	0.10

, whereas:

$$t_s = d_1+2b+c+d_2 \quad (1)$$

$$c = 0.400+0.005*(V_1+V_2) \quad (2)$$

$$d = 0.200+0.005*V_{1,2} \quad (3)$$

2.2 PEDESTRIAN PATHS

Pedestrian paths must have sufficient width not only to allow movement, but also to support free activities, the overall potential, and the attractiveness of the outdoor space. They have a key impact on urban life and accessibility for residents. They should be designed in a way that provides full physical protection from traffic lanes. In this sense, a sidewalk placed directly next to the edge of the roadway without a protective zone is, in every respect, the least safe solution. Pedestrians are highly sensitive to so-called “lateral obstacles,” which must be taken into account when defining the effective width of the path. The effective width of the path or the unobstructed pedestrian movement zone, directly depends on the physical and/or psychological barriers located on both sides of the path.

The minimum sidewalk width on streets within the primary urban network is **4.50 meters**.

Figure 2. Sidewalk zones

2.3 CYCLING PATHS AND LANES

The operating envelope of a cycling surface consists of the width of the bicycle (0.60 m) and the maneuvering space required on both sides (0.20 m each), totaling 1.00 m. The clearance envelope includes the operating envelope plus safety clearances on both sides of the bicycle, with a minimum of 0.25 m each. The safety distance between the bicycle's operating envelope and fences, street furniture, or greenery should be 0.25 m. The safety distance between the bicycle's operating envelope and the carriageway should range from 0.25 to 0.75 m for motor traffic speeds between 30 and 50 km/h. If there is parallel parking adjacent to the edge of the carriageway, this safety distance should be 0.75 m. On the primary urban street network, physical separation between bicycle and motor traffic is required. According to the European Cyclists' Federation (ECF), segregation of motor and bicycle traffic is necessary wherever motor traffic speeds are ≥ 50 km/h.

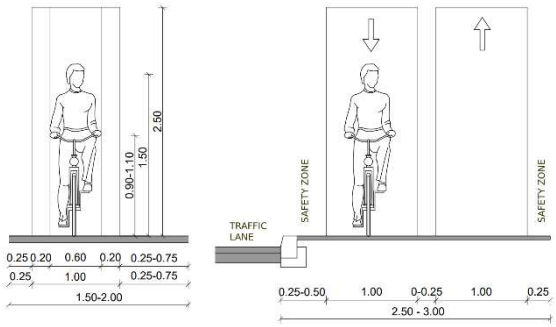

Figure 3. Cycling path, lane width

3. BOULEVARD "ST. CLEMENT OF OHRID" – SKOPJE

A typical example of a "grey street" is Boulevard "St. Clement of Ohrid" in Skopje. The boulevard is part of the primary urban street network of the City of Skopje, with a total length of approximately 917 meters. According to the functional classification of streets in the General Urban Plan (GUP) 2012–2022 of the City of Skopje, the boulevard is designated as an urban arterial street with a variable width ranging from 36 to 40 meters. This includes 2 x 10.50 m carriageways, a 5.00 m central green median, and sidewalks with variable widths ranging from 5.00 to 7.00 meters.

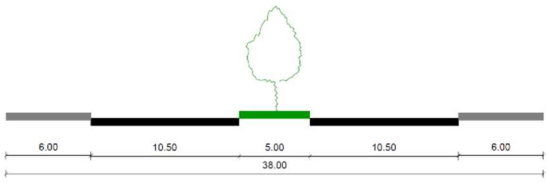

Figure 4. Cross-section of the boulevard according to the City of Skopje GUP 2012-2022

3.1 HISTORY OF THE BOULEVARD

The boulevard "St. Clement of Ohrid" is one of the oldest streets in the city, planned in the General Regulation Plan by architect Dimitrije T. Leko from 1914. In this plan, the areas on the left and right sides of the Stone Bridge are encircled by a boulevard called "Czar Dušan's Ring," which passes under the fortress through a tunnel. In the 1920s, street-related construction activities focused on expanding the existing street network and partially breaking through the "Czar Dušan" ring (today's "St. Clement of Ohrid" Boulevard).

Figure 5. "Czar Dušan's Ring" boulevard in the 1930s

In the period after World War II, the boulevard was preserved but underwent significant transformation of its surroundings with the construction of new residential and administrative buildings. It was renamed JNA Boulevard.

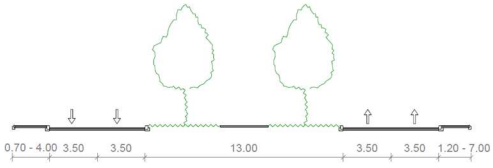

Figure 6. Cross-section of the boulevard up to 2011

In June 2011, a major reconstruction was carried out on the boulevard. An additional traffic lane was added at the expense of the central green strip, resulting in three traffic lanes per direction with a total width of 10.50 m. The two carriageway lanes are separated by a central green strip 5.00 m wide. The reconstruction also reorganized the existing intersections, creating dedicated left-turn lanes. At the intersection with Dimitrija Chupovski Street, the left-turn lanes were constructed, but left turns are prohibited.

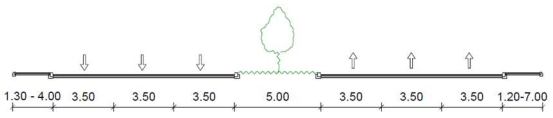

Figure 7. Cross-section of the boulevard up to 2011

In 2017, as part of the implementation of the new cycling infrastructure project "Skopje – Velograd," the width of the traffic lanes on a section of "St. Clement of Ohrid" Boulevard was reduced from 3.50 m to 3.00 m, enabling the introduction of one-way bicycle lanes in both directions with a width of 1.50 m each. "St. Clement of Ohrid" boulevard serves as one of the main connectors between routes 1, 2, and 3 of the "Skopje – Velograd" project.

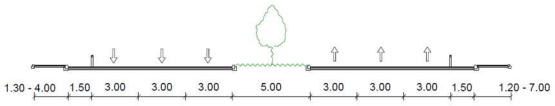

Figure 8. Cross-section of the boulevard from 2017 to the present

3.2 THE BOULEVARD TODAY

Although this boulevard is classified as an urban arterial street in the General Urban Plan of the City of Skopje, its cross-section does not correspond to its function.

CHARACTERISTICS OF AN URBAN ARTERIAL STREET	BOULEVARD "ST. CLEMENT OF OHRID"
They connect active areas of a city: residential zones with business districts, industrial zones, residential areas with the central urban area, and so on.	✗ connects individual parts of the central urban area.
They play a key role in public transport management.	✗ The boulevard plays a secondary role in the management of public urban transport.
Continuous traffic flow	✗ Interrupted traffic flow
Divided carriageways with at least two traffic lanes	▨ Divided carriageways with three traffic lanes
Pedestrian and bicycle paths separated from the carriageway by a planted curb strip	✗ Bicycle lanes on the carriageway and curb-separated bicycle and pedestrian paths
Urban buildings and facilities protected from noise and air pollution by a protective green strip.	✗ Curb built-up area

From the above, we can conclude that the cross-section of "St. Clement of Ohrid" Boulevard makes it a "grey street". Along and near the boulevard are located a university, cultural center, high school, cathedral, edge residential and business facilities, while at the same time it serves as a connection between Vodno and the Vardar River promenade, making it extremely important for pedestrian and bicycle traffic. Streets in the primary street network need to have a high-quality ambient function, which is especially important both for boulevard users and for the residents in its vicinity.

Figure 9. St. Clement of Ohrid Boulevard – Grey Street

Given the current situation, it is evident that the boulevard requires reconstruction aimed at increasing the safety of pedestrian and bicycle traffic, expanding urban greenery, reducing noise and air pollution, improving the boulevard's ambient function, and aligning the cross-section with its role in the street network. One way to achieve this goal is to reduce the number of traffic lanes to create space for protective curb green strips, two-way bicycle paths on both sides of the boulevard, and to widen pedestrian sidewalks where necessary.

3.3 CONCEPTUAL DESIGN

Typical cross-section of St. Clement of Ohrid Boulevard:
– Traffic lanes: 2 x 2 x 3.00 m
– Central median green strip: 3.00 m
– Bicycle paths: 2 x 2.50 – 2.75 m
– Curb green strips: 2 x 2.50 – 3.00 m
– Pedestrian sidewalks: 2 x 2.00 – 5.50 m

3.3.1 Intersections

At the intersection with Ilinden Boulevard, right-turn channelization has been eliminated to reduce crossing time for pedestrians and cyclists. Roughened surfaces are provided at the right-turn radii to slow down passenger vehicles while allowing larger motor vehicles—such as fire trucks, utility vehicles, ambulances, and similar to make turns. Within the intersection zone, continuous bicycle movements are ensured using a minimum turning radius of R = 3.00 m.

Figure 10. Pedestrian and bicycle crossing at the intersection with Ilinden Boulevard

For the intersection with Partizanski Odredi Boulevard, a solution has been developed involving the introduction of public transport on Partizanski Odredi Boulevard. The proposal includes implementing tramway public transport in the central part of the boulevard's cross-section. A tramway solution is presented, physically separated from the traffic lanes. Protective islands are planned between the right turns of motor vehicles and the bicycle lanes.

Figure 11. Intersection with Partizanski Odredi Boulevard

4. CONCLUSION

Modern urban street design represents a complex and comprehensive approach that prioritizes the needs of all users while integrating various elements to create safe, accessible, and vibrant public spaces. This entails creating conditions for multimodal transport, ensuring that streets provide safe motorized, pedestrian, and bicycle traffic.

Analyzing the current regulations in Macedonia and the widths of traffic lanes on urban roads in the country, especially in the city of Skopje, it is concluded that the lane widths rarely correspond to the maximum permitted speed in urban areas (50 km/h) and are most often dimensioned for higher speeds. In the General Urban Plan of the City of Skopje (2012–2022), 97% of the primary urban street network is planned with lane widths of 3.50 m, a width appropriate for speeds of 80–100 km/h. This data indicates that the city of Skopje needs to reduce the width of traffic lanes both in planning documentation and on existing roads to align the lane width with the maximum allowed speed of motor vehicles. Specifically, the lane widths on streets with at-grade intersections in urban areas should not exceed 3.00 m.

This adjustment will contribute to increased safety for all traffic participants, including pedestrians and cyclists, as well as drivers and passengers in motor vehicles.

In addition to increasing the safety of all types of traffic, reducing the width of traffic lanes on urban streets will also enable more rational dimensioning of the elements in the cross-section. The space gained by narrowing the traffic lanes can be used to introduce bicycle lanes or paths, widen pedestrian sidewalks, and increase green strips and areas, depending on the specific needs of the street. An indirect benefit of reducing lane widths is the reduction of asphalt surfaces, which contribute to the formation of urban heat islands and the increase of air temperature near the streets.

Figure 12. Transformation of St. Clement of Ohrid Boulevard

The historical changes to the cross-section of “St. Clement of Ohrid” Boulevard and the proposed solution can be seen in Figure 12 and reference [10].

REFERENCES

[1] Law On Traffic Safety, Official Gazette of the Republic of Macedonia No.169/2015,226/2015 and 55/2016, Article 35.

[2] General Urban Plan of the City of Skopje, Agency for Spatial Planning, City of Skopje, 2012.

[3] M. Maletin, Planiranje i Projektovanje Saobracajnica u Gradovima, Orion art, Beograd, 2009

[4] Rulebook on Standards and Norms for Design in the Republic of Macedonia, Official Gazette of the Republic of Macedonia 60/12, 29/15,32/16, 114/16 and Official Gazette of the Republic of North Macedonia 211/20.

[5] Rulebook for Technical Elements for the Construction and Reconstruction of Public Roads and Road Structures, Ministry of Transport and Communications, Official Gazette of the Republic of Macedonia 110/2009.

[6] Rulebook on Urban Planning, Ministry of Transport and Communications, Official Gazette of the Republic of North Macedonia 225/2020.

[7] O. Lindov, Sigurnost u cestovnom saobraćaju, Fakultet za saobraćaj i komunikacije, pp 110-112, Sarajevo, 2007.

[8] Speed Management: a Road Safety Manual for Decision-Makers and Practitioners, second edition. Global Road Safety Partnership, International Federation of Red Cross and Red Crescent Societies, Geneva; 2023.

[9] R. Sturtz, Cycling Lanes Reduce Fatalities for all Road Users, University of Colorado Denver, 2019.

[10] Ickovska, K., Трансформација на булевар Цв. Климент Охридски [Video]. YouTube. https://www.youtube.com/watch?v=_I1h-zyf6po&t=38s

Lan Hoang That Ton
PhD, Department of Civil Engineering
HCMC University of Architecture
Vietnam
tltechonlinesom@gmail.com
0000-0002-3544-917X

BUCKLING BEHAVIOR OF FUNCTIONALLY GRADED POROUS PLATE WITH PARABOLIC VARIABLE THICKNESS LAY ON PASTERNAK FOUNDATION: A MINI-STUDY

DOI: doi.org/10.55302/SJCE2514113tt

This article describes the buckling load of functionally graded porous plate with parabolic variable thickness (FGP-PVT) installed on Pasternak foundations. This construction also makes use of the sinusoidal porous distribution. With springer stiffness (k_1) and shear stiffness (k_2) as functions of the deflection and its Laplacian, the Pasternak foundation is a two-parameter model that depicts the foundation reaction. It is expected that the outcomes will offer information for the design of FGP-PVT plates in real-world engineering applications.

Keywords: buckling load, functionally graded porous plate, parabolic variable thickness, Pasternak foundation.

1. INTRODUCTION

Materials have always played a vital role in human existence. Certain properties result in particular uses. Materials for aircraft and aerospace applications have exceptional strength and low weight. When it comes to their capacity to possess novel characteristics and exceptional qualities that conventional materials cannot match, functionally graded materials (FGM) represent a wholly original idea [1]. Additive manufacturing is an efficient way to fabricate it [2, 3]. FGM structures must have mechanical performance, and it is important to look into how porosity affects this performance [4, 5]. The work [6] presented an effective approach to investigating the buckling and post-buckling behavior of porous functionally graded plates. The main objective of the analysis was to use a high-order continuity based on the asymptotic numerical method with the finite element method for nonlinear behaviors of a porous functionally graded material plate with different porosity distributions under various types of transverse

loads. A novel quasi-3D hyperbolic theory was presented for the free vibration analysis of functionally graded porous plates resting on elastic foundations by dividing transverse displacement into bending, shear, and thickness stretching parts as in [7]. The elastic foundation could be chosen as Winkler, Pasternak or Kerr foundation. Three different patterns of porosity distributions were considered. A Galerkin method was developed for the solution of the eigenvalue problem of this quasi-3D hyperbolic plate model. The bending and free vibration of porous functionally graded beams resting on elastic foundations were analyzed in [8]. The material features of the beam were assumed to vary continuously through the thickness according to the volume fraction of components. The foundation medium was also considered to be linear, homogeneous, and isotropic and modeled using the Winkler-Pasternak law. The hyperbolic shear deformation theory was applied for the kinematic relations, and the equations of motion were obtained using Hamilton's principle. The aim of the work [9] was to establish two-dimensional and quasi-three-dimensional shear deformation theories that could model the free vibration of functionally graded plates resting on elastic foundations using a new shear strain shape function. The proposed theories had a novel displacement field that included undetermined integral terms and contained fewer unknowns, taking into account the effects of both transverse shear and thickness stretching. The mechanical properties of the plates were assumed to vary through the thickness according to a power law distribution in terms of the volume fractions of the constituents. The elastic foundation parameters were introduced in the present formulation by following the Pasternak mathematical model. Hamilton's principle was employed to determine the equations of motion. The closed-form solutions were derived by using Navier's method, and then fundamental frequencies were obtained by solving the results of eigenvalue problems. The authors [10] gave a summary of the analytical and numerical techniques used to determine plates with functionally graded material properties that are supported by an elastic foundation. The finite elements method was used to obtain the numerical results, which were related to post-bifurcation problems of thermally loaded plates. The first-order shear deformation theory had been employed. In numerical calculations, they had used a new 16-node plate element, free of problems related to shear locking. The article [11] studied the effect of porosity distribution on the static and buckling responses of a functionally graded porous plate with all its four edges simply supported and subjected to a transverse load. The plate's displacement field was approximated based on an inverse hyperbolic shear deformation theory involving five variables. A numerical scheme for buckling analysis of a functionally graded circular plate (FGCP) subjected to uniform radial compression, including shear deformation, rested on a Pasternak elastic foundation was presented in [12]. The linear and quadratic thickness variation patterns with various boundary conditions were considered. A modified Euler-Lagrange equation was achieved and then solved by converting the differential equation to a nonlinear algebraic system of equations. Also, based on traction-free surface without using shear correction factor, a new approach by considering shear deformation for buckling analysis of FGCP rested on elastic foundation was carried out. The paper [13] presented a unified solution for free vibration analysis of thick functionally graded porous graphene platelet-reinforced composite cylindrical shells embedded in elastic foundations. The three-dimensional theory of shell theory was introduced for theoretical formulation. The Rayleigh-Ritz method in conjugation with the artificial spring technique was employed, where the arbitrary boundary conditions could be conveniently obtained. A unified solution that comprises six different displacement functions was developed. Several other similar studies can be listed here [14-22]. The study [14] was to further expand the ES-MITC3 for analyzing the buckling characteristics of functionally graded porous variable-thickness plates with sinusoidal porous distribution. The ES-MITC3 was developed to improve the accuracy of classical triangular elements (Q3) and overcome the locking phenomenon while still ensuring flexibility in discretizing the structural domain of the Q3. The bending responses of porous functionally graded thick rectangular plates were investigated in [15] according to a high-order shear deformation theory. Both the effects of shear strain and normal deformation were included in the present theory, so it did not need any shear correction factor. The equilibrium equations according to the porous functionally graded plates were derived. The solution to the problem was derived by using Navier's technique. In the investigation [16], the buckling behaviors of porous double-layered functionally graded nanoplates in a hygrothermal environment were presented. The nonlocal strain gradient theory with two material scale parameters was developed to

examine buckling behavior much more accurately. Based on the new first-order shear deformation theory, the equations of equilibrium were obtained from the principle of minimum potential energy. To simplify the equations of equilibrium and remove the bending-extension coupling, the buckling behaviours of FG nanoplates were investigated based on the physical neutral surface concept. The paper [17] introduced a simple quasi-3D theory with Reddy shear function and a new trigonometric shear function to conduct free vibration analysis of the functionally graded plates resting on Winkler/Pasternak/Kerr elastic foundation. The proposed transverse shear strain functions satisfied the stress-free boundary conditions on the surfaces of the functionally graded plate without using any shear correction factors. The governing differential equation and boundary conditions were derived based on Hamilton's principle and the Winkler/Pasternak/Kerr type mathematical model. Vibration analysis of a functionally graded rectangular plate resting on a two-parameter elastic foundation was presented in [18]. The displacement field based on the third-order shear deformation plate theory was used. By considering the in-plane displacement components of an arbitrary material point on the mid-plane of the plate and using Hamilton's principle, the governing equations of motion were obtained, which are five highly coupled partial differential equations. An analytical approach was employed to decouple these partial differential equations. The decoupled equations of a functionally graded rectangular plate resting on an elastic foundation were solved analytically for Levy type boundary conditions. The new numerical procedure for functionally graded skew plates in a thermal environment was presented in the study [19] based on the C0-form of the novel third-order shear deformation theory. Without the shear correction factor, the theory was also taking the desirable properties and advantages of the third-order shear deformation theory. The author assumed that the uniform distribution of temperature was embedded across the thickness of the structure. Both the rule of mixture and the micromechanics approaches were considered to describe the variation of material compositions across the thickness. For thermo-mechanical analysis of functionally graded sandwich plates supported by a two-parameter (Pasternak model) elastic foundation, a refined quasi-three-dimensional shear deformation theory was developed in the paper [20]. Unlike the other higher-order theories, the number of unknowns and governing equations of this theory was only four against six or more unknown displacement functions used in the corresponding ones. Furthermore, the theory took into account the stretching effect due to its quasi-three-dimensional nature. The boundary conditions in the top and bottom surfaces of the functionally graded plate were satisfied, and no correction factor was required. The paper [22] presented an analytical investigation of the vibrations of porous functionally graded carbon nanotube-reinforced composite plates resting on elastic foundations. The plates were reinforced with randomly oriented straight carbon nanotubes, featuring four distinct reinforcement distribution patterns along the thickness. Material properties of the structure were graded along the thickness, with both symmetric and asymmetric porosity distributions considered. Utilizing high-order shear deformation theory, the equations of motion were derived from Hamilton's energy principle, and Navier's method was employed for the solutions. A physics-informed neural network method based on a two-network strategy was introduced in [23] to address the bending problem of thin plates with variable stiffness resting on an elastic foundation. The problem was governed by a fourth-order partial differential equation (PDE), and the use of a one-network strategy to solve the PDE directly might lead to convergence issues due to singular points. Following the principles of Kirchhoff plate theory, the governing PDE was equivalently transformed into four second-order PDEs. A two-network strategy was employed for solution. The authors presented numerical examples under various load conditions, plate geometries, foundation types, thicknesses, and material properties. The obtained results were validated against finite element method solutions and literature. The study [24] aimed to investigate the method of fundamental solution to the thin plate resting on the elastic foundation subjected to in-plane forces under either static or dynamic load. The fundamental solutions with Bessel's functions were derived in both static and dynamic cases. According to the principle of superposition, the boundary conditions were satisfied at collocation points in terms of densities of concentrated force at source points outside the domain. A double-source algorithm and a single-source algorithm were proposed to deal with fourth-order partial differential equations. Based on the symplectic superposition method, the T-shaped thin plate on the Winkler elastic foundation was divided into four sub-plates and solved by using the

symplectic eigen expansion method, and the modes and frequencies were studied. The method began directly with the fundamental equations and a rigorous mathematical derivation without assuming the form of the solution beforehand. The approach helped circumvent the drawbacks associated with traditional semi-inverse solution methods. In addition, the theoretical calculation model and finite element analysis model of T-shaped thin plates on elastic foundation were established by using Mathematic software and ABAQUS software in paper [25]. In the research [26], the nonlinear dynamics of a clamped circular composite plate placed on a softening elastic foundation under rapid thermal loading was investigated. In the situation, based on the amount of temperature supplied to the structure and the coefficients of softening elastic foundation, two instabilities might happen one after the other. The structure would thermally buckle and deform dynamically if the applied temperature exceeded a critical level. If the softening coefficient of the elastic foundation was critical, the structure would completely lose its stability after a certain deformation range. A polymer containing graphene platelets made up the system. Based on various functions, the volume fraction of fillers varied along the thickness. The system's nonlinear dynamic equations were obtained by applying Hamilton's principle and the Von-Kármán theory. The transient heat conduction equation was solved by the cubic B-spline collocation and Crank-Nicolson procedures. A nonlinear numerical analysis regarding a functionally graded carbon nanotube-reinforced composite plate on an elastic foundation was carried out in [27]. The large deflection bending problem was formulated according to the von Kármán nonlinear theory and the hierarchical model. Additionally, the 2D natural element method—which demonstrated a high degree of accuracy even for coarse grid—was used to solve it numerically. The load increment scheme and the Newton-Raphson iteration method were combined to iteratively calculate the derived nonlinear matrix equations. The authors investigated impact analysis of functionally graded graphene nanoplatelets reinforced composite plates with arbitrary boundary conditions and resting on Winkler-Pasternak elastic foundations as in [28]. The element-free improved moving least-squares Ritz approach and the higher-order shear deformation theory were used to develop the theoretical formulation. Target plates were set to have uniform and functionally graded graphene nanoplatelet distributions throughout their thickness. The modified Halpin-Tsai model was considered to calculate the effective Young's modulus, yet the rule of mixture was used to calculate the effective Poisson's ratio and mass density. The modified nonlinear Hertz contact law was adopted to describe the contact force between the spherical impactor and target plates. The elastic buckling problem of a thin skew isotropic plate under in-plane loading resting on the Pasternak elastic foundation was numerically solved in [29] using the extended Kantorovich method (EKM). EKM had never been applied to this problem before. An investigation of the EKM accuracy and convergence was conducted. Formulations were based on classical plate theory. Using the variational calculus expressed in an oblique coordinate system, stability equations and boundary conditions terms were obtained from the principle of the minimum total potential energy. The resulting two sets of ordinary differential equations were solved numerically using the Chebfun package in Matlab software. The article [30] investigated the bending response performances of the magneto-electro-elastic laminated plates supported by the Winkler foundation or the elastic half-space under transverse mechanical loading. Assuming that the foundation was not electrically and magnetically conductive, the magneto-electro-elastic laminated plate and the elastic half-space were simulated using the scaled boundary finite element method based on the 3D theory of elasticity. Only the in-plane of the magneto-electro-elastic laminated plate or the boundary of the elastic half-space needs to be discretized, reducing the spatial dimension by one. This was due to the fact that the generalized displacement involving the electric potential, magnetic potential, and elastic displacement was considered as the nodal degree of freedom for the magneto-electro-elastic laminated plates in the scaled boundary finite element method model. Furthermore, the governing equations could be solved analytically in the radial direction of the scaled coordinate system, which made the scaled boundary finite element method particularly suitable for simulating the elastic half-space. The global stiffness coupling governing equation for the Winkler foundation-plate system was directly derived from the 3D elasticity equations of the magneto-electro-elastic laminated plate. This equation took into account the interaction between the Winkler foundation and the magneto-electro-elastic laminated plate and assumed that the foundation reactions were proportionate to the

transverse displacements of the plate structure. However, the entire domain was divided into three sub-domains for the magneto-electro-elastic laminated plate-half-space system: the scaled boundary finite element method, the magneto-electro-elastic laminated plate structure, and the near and semi-infinite far foundation systems. This allowed for the determination of the stiffness matrix of each sub-domain. Therefore, the global stiffness equation of the plate-half-space system could be assembled at the same nodes using the degree of freedom matching principle. The paper [31] dealt with the impacts of temperature and moisture on the bending behavior of functionally graded porous plates resting on elastic foundations. The impacts of transverse shear deformation as well as the transverse normal strain were taken into consideration. The number of unknown functions involved here was only five, as opposed to six or more in the case of other shear and normal deformation theories. The effects due to side-to-thickness ratio, aspect ratio, thermal and moisture loads, porosity factor, and elastic foundation parameters, as well as the volume fraction distribution on the functionally graded porous plates, were investigated. The study conducted in [32] examined the vibration of orthotropic plates with bidirectional exponential grade resting on a two-parameter elastic foundation. The Pasternak elastic foundation model was used as a two-parameter foundation model. The heterogeneity of the orthotropic exponentially changed depending on the axial and thickness coordinates. The motion equation was derived based on the classical plate theory and solved by using the Galerkin method. A comparison with earlier research was done in order to validate the findings. The effects of the two-parameter elastic foundations, material gradient, and orthotropy on the dimensional frequency parameters were examined. The local buckling behavior of long rectangular plates supported by tensionless elastic Winkler foundations and subjected to a combination of uniform longitudinal uniaxial compressive and uniform in-plane shear loads was analytically solved using a mathematical approach in the paper [33]. Fitted formulas were derived for plates with clamped edges and simplified supported edges. Two examples were given to demonstrate the application of the current method: one was a plate on tensionless spring foundations, and the other was the contact between the steel sheet and elastic solid foundation, etc.

The FGP-PVT plate formulation is taken into consideration to start this investigation, particularly with regard to porosity appearance. The article concludes with some notes after the approximate solution pertaining to buckling behavior is calculated using Matlab software.

2. FORMULATION

A functionally graded porous plate *a*×*b* with parabolic variable thickness (FGP-PVT) is presented in Figure 1. The effective material properties $M(z)$ through the thickness h can be expressed as

$$M(z)=\left[\left(M_c - M_m\right)V_c(z)+M_m\right]\times \times\left[1-e_0\cos\left(\frac{\pi z}{h(x)}\right)\right] \quad (1)$$

with

$$V_c(z)=\left(\frac{z}{h(x)}+\frac{1}{2}\right)^n \quad \text{for} \quad z\in\left[-\frac{h(x)}{2},\frac{h(x)}{2}\right] \quad (2)$$

$$h(x)=h_0\left[1+\left(\frac{x}{a}\right)^2\right] \quad (3)$$

and e_0 is porosity factor, n is the power-law index, symbols m and c represent the metal and ceramic constituents.

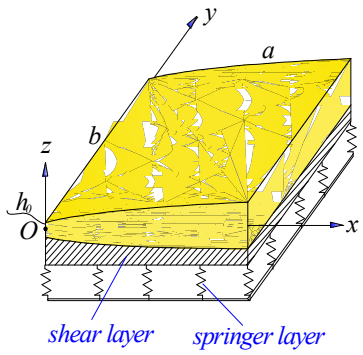

Figure 1. The FGPPVT plate resting on Pasternak foundation

Pasternak's model is determined by

$$\Omega=k_1 w(x,y)-k_2\left[\left(\frac{\partial w}{\partial x}\right)^2+\left(\frac{\partial w}{\partial y}\right)^2\right] \quad (4)$$

with k_1 is springer stiffness and k_2 is shear stiffness. Reddy's C^0-TSDT is used to express the plate's displacement field as follows

$$u(x,y,z)=u_0+\left(z-\frac{4z^3}{3h^2(x,y)}\right)\beta_x - \frac{4z^3}{3h^2(x,y)}\phi_x \quad (5)$$

$$v(x,y,z)=v_0+\left(z-\frac{4z^3}{3h^2(x,y)}\right)\beta_y - \frac{4z^3}{3h^2(x,y)}\phi_y \quad (6)$$

$$w(x,y,z)=w_0 \quad (7)$$

Using a four-node quadrilateral element with seven degrees of freedom for each node u_0, v_0, w_0, β_x, β_y, ϕ_x and ϕ_y for finite element procedure similar to the literature [15-21] and finding the buckling load.

3. THE APPROXIMATE SOLUTION

For example, the material properties can be seen in Table 1.

Table 1. The material properties

Al_2O_3	E_c = 380 GPa	ν_c = 0.3	ρ_c = 3800 kg/m^3
Al	E_m = 70 GPa	ν_m = 0.3	ρ_m = 2707 kg/m^3

Firstly, the *a/b* ratio gets values 0.5, 1 & 2 with remaining parameters as h_0=*a*/60, $\bar{k}_1=75$ and $\bar{k}_2=15$. The dimensionless values are presented by

$$\bar{N}_{cr}=\frac{N_{cr}a^2}{E_m h^3},\ \bar{k}_1=\frac{k_1 a^4}{D},\ \bar{k}_2=\frac{k_2 a^2}{D} \text{ with } D=\frac{E_m h^3}{12\left(1-\nu_m^2\right)}.$$

The buckling loads of the (SCSC) FGP-PVT rectangular plates are shown in Table 2 and compared with other solutions from [14]. It can be seen that the increases in *n* or e_0 reduces the load $\bar{N}_{cr}$. Table 3 further lists the buckling loads of FGP-PVT square plates with input parameters: h_0 =*a*/55, e_0 = 0.2 and *n* = 10.

Table 2. The comparison of buckling load $\bar{N}_{cr}$

a/b	*n*	e_0					
		0		0.2		0.4	
		[14]	Present	[14]	present	[14]	present
0.5	0	47.2858	47.3557	43.9859	44.0713	40.6807	40.6667
			0.148%		*0.194%*		*-0.034%*
	2	19.6898	19.9104	18.2596	18.4326	16.7933	16.8321
			1.120%		*0.947%*		*0.231%*
	4	17.3742	17.2634	16.2219	16.1788	15.0427	14.9238
			-0.638%		*-0.266%*		*-0.790%*
1	0	64.8525	65.1179	60.3002	60.8337	55.7386	*55.7142*
			0.409%		*0.885%*		*-0.044%*
	2	26.8777	26.7915	24.9055	24.8712	22.8831	22.6333
			-0.321%		*-0.138%*		*-1.092%*
	4	23.6810	23.7068	22.0922	22.1004	20.4658	20.5885
			0.109%		*0.037%*		*0.599%*
2	0	148.3186	149.4774	137.5344	138.2654	126.7048	127.0001
			0.781%		*0.531%*		*0.233%*
	2	59.7360	60.1206	55.0820	55.1333	50.3075	50.4417
			0.644%		*0.093%*		*0.267%*
	4	52.1433	52.1399	48.3993	48.4189	44.5657	44.3279
			-0.007%		*0.040%*		*-0.534%*

Table 3. The buckling loads $\bar{N}_{cr}$ of FGP-PVT square plates

BCs	$\bar{k}_1$	$\bar{k}_2$	Buckling load
SSSS	0	0	*2.4137*
	100	0	*3.2104*
	100	10	*4.6994*
CCCC	0	0	*6.0783*
	50	0	*6.3528*
	50	5	*7.1067*

4. CONCLUSION

In this article, the buckling load of the FGP-PVT plate is shown. The results of this article are approximate with other solutions in references. The results obtained are anticipated to provide valuable insights for the design of FGP-PVT plates in practical engineering applications.

REFERENCES

[1] A. Pasha and B. M. Rajaprakash (2022), “Fabrication and mechanical properties of functionally graded materials: A review”, *Materials Today: Proceedings*, 52, 379-387.

[2] E. J. Kim, C. M. Lee and D. H. Kim (2023), “Study on the characteristics of functionally graded materials from Ni-20cr to Ti-6Al-4V via directed energy deposition”, *Journal of Alloys and Compounds*, 955, 170263.

[3] D. D. Singh, S. Arjula and A. R. Reddy (2021), “Functionally graded materials manufactured by direct energy deposition: A review”, *Materials Today: Proceedings*, 47, 2450-2456.

[4] Y. Xiong, Z. Han, J. Qin, L. Dong, H. Zhang, Y. Wang, H. Chen and X. Li (2021), “Effects of porosity gradient pattern on mechanical performance of additive manufactured Ti-6Al-4V functionally graded porous structure”, *Materials & Design*, 208, 109911.

[5] D. Khrapov, M. Kozadayeva, A. Koptyug, T. Mishurova, D. Meinel, R. Surmenev and M. Surmeneva (2023), “Geometrical features and mechanical properties of the sheet-based gyroid scaffolds with functionally graded porosity manufactured by electron beam melting”, *Materials Today Communications*, 35, 106410.

[6] H. Chaabani, S. Mesmoudi, L. Boutahar and K. E. Bikri (2023), ”A high-order finite element continuation for buckling analysis of porous FGM plates”, *Engineering Structures*, 279, 115597.

[7] D. Shahsavari, M. Shahsavari, L. Li and B. Karami (2018), “A novel quasi-3D hyperbolic theory for free vibration of FG plates with porosities resting on Winkler/Pasternak/Kerr foundation”, *Aerospace Science and Technology*, 72, 134-149.

[8] L. Hadji, F. Bernard and N. Zouatnia (2022), “Bending and Free Vibration Analysis of Porous-Functionally-Graded (PFG) Beams Resting on Elastic Foundations”, *Fluid Dynamics and Materials Processing*, 19(4), 1043-1054.

[9] F. Z. Zaoui, D. Ouinas and A. Tounsi (2019), “New 2D and quasi-3D shear deformation theories for free vibration of functionally graded plates on elastic foundations”, *Composites Part B: Engineering*, 159, 231-247.

[10] M. Taczała, R. Buczkowski and M. Kleiber (2015), “Postbuckling analysis of functionally graded plates on an elastic foundation”, *Composite Structures*, 132, 842-847.

[11] M. Dhuria, N. Grover and K. Goyal (2021), “Influence of porosity distribution on static and buckling responses of porous functionally graded plates”, *Structures*, 34, 1458-1474.

[12] A. Heydari, A. Jalali and A. Nemati (2017), “Buckling analysis of circular functionally graded plate under uniform radial compression including shear deformation with linear and quadratic thickness variation on the Pasternak elastic foundation”, *Applied Mathematical Modelling*, 41, 494-507.

[13] B. Qin, Q. Wang, R. Zhong, X. Zhao and C. Shuai (2020), “A three-dimensional solution for free vibration of FGP-GPLRC cylindrical shells resting on elastic foundations: a comparative and parametric study”, *International Journal of Mechanical Sciences*, 187, 105896.

[14] T.T. Nguyen, T.S. Le, T.T. Tran and Q.H Pham (2024), “Buckling analysis of functionally graded porous variable thickness plates resting on Pasternak foundation using ES-MITC3”, *Latin american journal of solids and structures*, 21(2), e524.

[15] S. Merdaci and H. Belghoul (2019), "High-order shear theory for static analysis of functionally graded plates with porosities", *Comptes Rendus Mécanique*, 347(3), 207-217.

[16] N. Radić (2018), "On buckling of porous double-layered FG nanoplates in the Pasternak elastic foundation based on nonlocal strain gradient elasticity", *Composites Part B: Engineering*, 153, 465-479.

[17] M. Li, C. G. Soares and R. Yan (2021), "Free vibration analysis of FGM plates on Winkler/Pasternak/Kerr foundation by using a simple quasi-3D HSDT", *Composite Structures*, 264, 113643.

[18] A.H. Baferani, A.R. Saidi and H. Ehteshami (2011), "Accurate solution for free vibration analysis of functionally graded thick rectangular plates resting on elastic foundation", *Composite Structures*, 93(7), 1842-1853.

[19] H.L. Ton-That (2020, "Finite element analysis of functionally graded skew plates in thermal environment based on the new third-order shear deformation theory", *Journal of Applied and Computational Mechanics*, 6(4), 1044-1057.

[20] A. Mahmoudi, S. Benyoucef, A. Tounsi, A. Benachour, E.A.A. Bedia and S.R. Mahmoud (2019), "A refined quasi-3D shear deformation theory for thermo-mechanical behavior of functionally graded sandwich plates on elastic foundations", *Journal of Sandwich Structures & Materials*, 21(6), 1906–1929.

[21] L.H.T Ton (2021), “A modified shear deformation theory associated with the four-node quadrilateral element for bending and free vibration analyses of plates”, *International Journal of Engineering and Applied Physics*, 1(3), 235–241.

[22] T.S Tayeb, M. Amir, S.W Kim and D. Choi (2024), "An analytical modelling of free vibration in porous FG-CNTRC plate resting on elastic foundations", *Materials Today Communications*, 40, p. 109925.

[23] L.X Peng, J.K Sun, Y.P Tao and Z.M Huang (2024), "Bending analysis of thin plates with variable stiffness resting on elastic foundation via a two-network strategy physics-informed neural network method", *Structures*, 68, p. 107051.

[24] M.X Wang, X.B Yan, Y.C Liu and P.H Wen (2024), "Method of fundamental solution for thin plate resting on elastic foundation with in-plane forces", *Engineering Analysis with Boundary Elements*, 164, p. 105767.

[25] H.J Jiang, Q.Z Guo, X.G Wang and N.H Gao (2024), "Comparison of free vibration behaviors for simply supported and clamped T-shaped thin plate resting on Winkler elastic foundation", *Thin-Walled Structures*, 197, 111621.
[26] Z. Dai, H. Tang, S. Wu, M. Habibi, Z. Moradi and H.E Ali (2023), "Nonlinear consecutive dynamic instabilities of thermally shocked composite circular plates on the softening elastic foundation", *Thin-Walled Structures*, 186, p. 110645.
[27] J.R Cho (2022), "Nonlinear bending analysis of FG-CNTRC plate resting on elastic foundation by natural element method", *Engineering Analysis with Boundary Elements*, 141, pp. 65-74.
[28] B.A Selim and Z. Liu (2021), "Impact analysis of functionally-graded graphene nanoplatelets-reinforced composite plates laying on Winkler-Pasternak elastic foundations applying a meshless approach", *Engineering Structures*, 241, p. 112453.
[29] A.H.A. Hassan and N. Kurgan (2020), "Buckling of thin skew isotropic plate resting on Pasternak elastic foundation using extended Kantorovich method", *Heliyon*, 6(6), e04236.
[30] W. Ye, J. Liu, H. Fang and G. Lin (2020), "Numerical solutions for magneto–electro–elastic laminated plates resting on Winkler foundation or elastic half-space", *Computers & Mathematics with Applications*, 79(8), pp. 2388-2410.
[31] D.S Mashat, A.M Zenkour and A.F Radwan (2020), "A quasi-3D higher-order plate theory for bending of FG plates resting on elastic foundations under hygro-thermo-mechanical loads with porosity", *European Journal of Mechanics - A/Solids*, 82, p. 103985.
[32] V.C Haciyev, A.H Sofiyev and N. Kuruoglu (2018), "Free bending vibration analysis of thin bidirectionally exponentially graded orthotropic rectangular plates resting on two-parameter elastic foundations", *Composite Structures*, 184, pp. 372-377.
[33] J. Dong, X. Ma, Y. Zhuge and J.E Mills (2018), "Local buckling of thin plate on tensionless elastic foundations under interactive uniaxial compression and shear", *Theoretical and Applied Mechanics Letters*, 8(2), pp. 75-82.

Mohammad Kamruzzaman Talukder
PhD, Assistant Professor
Department of Civil Engineering
East West University, Dhaka
Bangladesh
mktalukder@ewubd.edu
0009-0003-4502-2609

APPLICATION OF C++ COMPUTER PROGRAMMING TO INCREMENTAL STRESS UPDATE PROCEDURE FOR NUMERICAL IMPLEMENTATION OF THE MODIFIED CAM-CLAY CONSTITUTIVE MODEL – A CONTRIBUTION TO THE TEACHING OF GEOMECHANICS

DOI: doi.org/10.55302/SJCE2514121kt

Teaching the computation of soil stress-strain responses presents a significant challenge in geomechanics education. Over the past decade, modern programming languages, particularly C++, have been integrated into the curricula of undergraduate and graduate engineering programs to facilitate the application of numerical methods in geomechanics. Among the various models used to predict the nonlinear response of soil to monotonic stress, the modified Cam-clay (MCC) soil plasticity model is widely recognized and taught in geomechanics courses at engineering institutions worldwide. However, the numerical implementation of the MCC model using contemporary programming languages within the framework of the Invariants of Stress Tensor is not extensively documented in publicly available resources. This study addresses this gap by numerically solving the MCC model through the Invariants of Stress Tensor, employing the Gauss Elimination method and the Incremental Stress Update Method. Additionally, a flow chart is included to illustrate the implementation process.

Keywords: Modified Cam-clay, Stress path, Gauss elimination, yield surface, Incremental Stress Update procedure, plastic strain, shear strain, volumetric strain.

1. INTRODUCTION

In this study, the modified cam-clay (MCC) plasticity model of critical state soil mechanics is selected for the stress-strain response and

stress path computations. Computer C++ programming is used to implement the stress-strain computation algorithms for the MCC model that can take into account soil elastoplasticity. The MCC model is implemented using the incremental stress update (ISU) method, which can solve a system of linear algebraic equations relating stress increments to strain increments.

The ISU method used by Hashiguchi et al. (Hashiguchi, Saitoh, & Okayasu, 2002) is implemented in the study for numerical test of the MCC model. In the ISU method, an incremental strain vector is calculated by solving elastoplastic constitutive relations of the MCC model with Gauss elimination technique (Hashiguchi, Saitoh, & Okayasu, 2002). By multiplying the stress-strain matrix with the incremental strain matrix, incremental stresses are directly updated once the MCC model's yield criterion has been met. In this procedure, the approximate solution for the stresses diverge from the analytical solution after a number or stress increments. In the study, the linear algebraic equations are solved using Gauss elimination technique (GET) for unknown stress and strain values. Stress-strain response and stress path computed in the study are compared with PLAXIS numerical triaxial test results and analytical closed form solutions. The stress-strain response and stress path response calculated with the ISU method compares well with the PLAXIS simulation results and analytical solution. This study uses a few soil parameters that can be obtained from straightforward geotechnical drained and undrained triaxial tests at a variety of working loads of interest rather than just loads at failure to accurately predict the stress-strain response. The C++ computer program is provided in the paper in order to facilitate the teaching and learning numerical methods in geomechanics at graduate schools across the world.

To fully comprehend how the study implemented the MCC elastoplastic model using the incremental ISU method, we need to review literature on non-linear elasto-plastic stress analysis. The literature include concepts of general elasticity and plasticity of soils.

1.1 MODELING OF GEOMATERIAL RESPONSE

Stress-strain response of geomaterials can be obtained by experimental methods but experimental methods are time consuming and at times can be inaccurate because of sample disturbances. Soil constitutive modeling is a branch of geomechanics, where numerical methods are used to accurately describe experimentally observed stress-strain responses, for example, irreversible deformation and yield phenomena of soils and rock under both static and dynamic loading conditions. However, using mathematical relations to predict the response of geomaterials under all possible loading conditions is not always possible The following requirements must be met for a numerical model of the stress-strain response of geomaterials to be useful.

The material response model should be able to predict the material behavior for all stress and strain paths and not just a single class of paths (for example, axial symmetry or pure shear). A small number of straightforward geotechnical laboratory tests should be enough to estimate the model's parameters. Elastoplastic nonlinear soil response to loading and unloading conditions (stress history) should be predicted by the model.

Many of the aforementioned characteristics of material models have been successfully described using elasto-plasticity models based on critical state formulation. Soil hardening, softening, and stress history are all included in the MCC, a critical state-based model with 3D stress and strain calculations. The MCC model requires few model parameters which can be directly obtained from standard oedometer and conventional tri-axial compression tests.

1.2 LINEAR ELASTIC MATERIAL

Stress-strain response of isotropic linear elastic materials are described by the following relationships:

Incremental volumetric strain in a soil element,

$$d\varepsilon_v = \frac{1}{K'} dp \quad (1)$$

where, K'=bulk modulus of soil

dp = incremental mean effective pressure on a soil element

Incremental shear strain

$$d\varepsilon_s = \frac{1}{3G} dq \quad (2)$$

where, G = shear modulus of soil and ε_s is the shear strain.

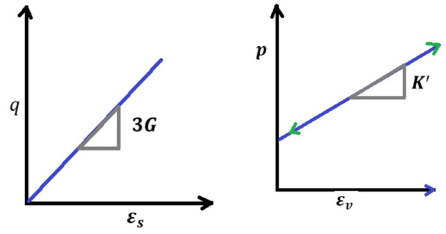

a) shearing (b) Isotropic compression and swelling

Figure 1: Behavior of isotropic linear elastic material

In matrix form

$$\begin{bmatrix} d\varepsilon_v \\ d\varepsilon_s \end{bmatrix} = \begin{bmatrix} \frac{1}{K'} & 0 \\ 0 & \frac{1}{3G} \end{bmatrix} \begin{bmatrix} dp \\ dq \end{bmatrix} \quad (3)$$

1.3 INELASTIC SOIL MATERIAL

Soils are considered inelastic materials because they only behave elastically for strains typically less than 10^{-5}. For most soils, the elastic response is only a small part of the overall deformation and the response can be significantly different in relation to that predicted by elastic theory. Inelastic soils exhibit the following features:

Elastic and plastic (i.e., inelastic) deformation components of total strain are independent

$$\boldsymbol{\varepsilon^t = \varepsilon^e + \varepsilon^p} \quad (4)$$

1.4 YIELD FUNCTIONS FOR INELASTIC MATERIAL

A yield function mathematically expresses every possible combination of biaxial or triaxial stresses that can cause inelastic material to yield. The yield surface of an elastoplastic material is fixed in stress space. First, let us look at the yield surface below in biaxial stress space.:

$$\boldsymbol{df = 0; f = f_c} \quad (5)$$

$$\boldsymbol{f(\sigma_{ij}) = f_c} \quad (6)$$

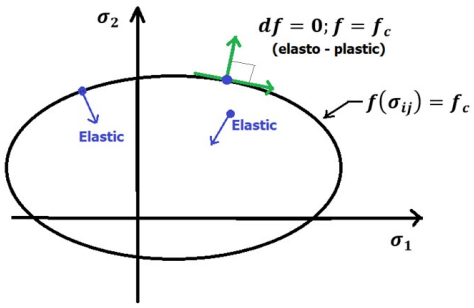

Figure 2: Schematic yield surface for a perfectly plastic material response to biaxial loading

In general the initial yield function for stress-strain response of elast0-plastic material can be described as below:

$$\boldsymbol{f(\sigma_{ij}) = f_c} \quad (7)$$

For all stress states within the yield surface the yielded material will behave elastically. The loading condition for elastic response is given by

$$\boldsymbol{f < f_c} \quad (8)$$

If the stress state coincides with the yield locus then and only then, plastic strain will occur. Thus, the loading condition for plastic behavior is given by:

$$\boldsymbol{f = f_c} \quad (9)$$

$$\boldsymbol{df = \frac{\partial f}{\partial \sigma_{ij}}} \quad (10)$$

If a stress path originates from the yield locus, the loading condition is given by;

$$\boldsymbol{f = f_c} \quad (11)$$

$$\boldsymbol{df = \frac{\partial f}{\partial \sigma_{ij}} d\sigma_{ij} < 0} \quad (12)$$

1.5 FLOW RULE AND HARDENING LAW

The ratio of incremental plastic shear strain to incremental plastic volumetric strain is used to express the direction of an incremental plastic strain vector. The relationship between the state of stress and the direction of the vector of plastic strain is known as flow rule. A flow rule defines the relationship between the net increment of the plastic strain increment $\boldsymbol{\varepsilon_{ij}^p}$, and the present state of stress $\boldsymbol{\sigma_{ij}}$.

Increased yield stress level due to plastic straining is called material hardening. The relationship between the increase in the yield stress and plastic strain is known as hardening law.

$$\boldsymbol{g\left(\sigma_{ij}, \varepsilon_{ij}^{p}\right) = 0} \quad (13)$$

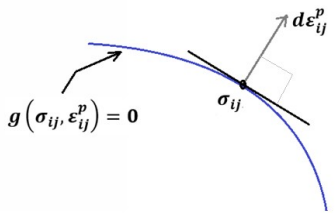

Figure 3: Representation of flow rule

Incremental plastic strain is expressed (Chen & Mizuno, 1990) below

$$\boldsymbol{d\varepsilon_{ij}^{p} = d\lambda \frac{dg}{d\sigma_{ij}}} \quad (14)$$

In above equation $\boldsymbol{d\lambda}$ is a positive scalar proportionality quantity which is dependent on the state of stress and loading history. If the plastic potential surface and yield surface coincide with each other, then, it is $\boldsymbol{f = g}$, the flow rule is called the associated flow rule; otherwise it is the non-associated type. It can be seen in the equation of flow rule, the direction of the plastic strain increment vector $\boldsymbol{d\varepsilon_{ij}^{p}}$, is normal to the plastic potential surface g at the current stress point $\boldsymbol{\sigma_{ij}}$ which is known as normality condition. Normality rule is more appropriate for clay and less so for sand.

1.6 PLASTIC WORK

Plastic work done per unit volume of a deformable elasto-plastic material during a strain increment $d\varepsilon$ is given by;

$$\boldsymbol{dW = \sigma_{ij} d\varepsilon_{ij}} \quad \textbf{(15)}$$

where, $d\varepsilon_{ij}$ is the total strain increment. This consists of both elastic and plastic components. It can be decomposed as;

$$\boldsymbol{d\varepsilon_{ij} = d\varepsilon_{ij}^{e} + d\varepsilon_{ij}^{p}} \quad (16)$$

Therefore, $\boldsymbol{dW}$ is given by

$$\boldsymbol{dW = \sigma_{ij}\left(d\varepsilon_{ij}^{e} + d\varepsilon_{ij}^{p}\right)} \quad (17)$$
$$\boldsymbol{= \sigma_{ij} d\varepsilon_{ij}^{e} + \sigma_{ij} d\varepsilon_{ij}^{p}}$$
$$\boldsymbol{= dW^{e} + dW^{p}}$$

Where, dW^{e} is the recoverable elastic energy and dW^{p} is the plastic work.

1.7 CONCEPT OF CRITICAL VOID RATIO

When a loose sand or normally consolidated clay is sheared, it passes through progressive states of yielding before failure. That is, plastic deformations occur as the stress path passes through multiple yield surfaces. The material will continue to yield until it reaches a critical void ratio, at which point the void ratio won't change during subsequent shearing. That is, during shearing, the material reaches a point where the packing of the particles is such that there is no change in volume (Wood, 1991). This particular void ratio is called the critical void ratio. This can be considered as the critical state of the material (Wood, 1991). At the point when a dense sand or heavily overconsolidated clay is sheared, it reaches a peak stress and afterward reaches a residul stress. It is hown in figure below that, the material volume initially decreases, then dilates until the volumetric strain reaches a constant value which corresponds to its critical value.

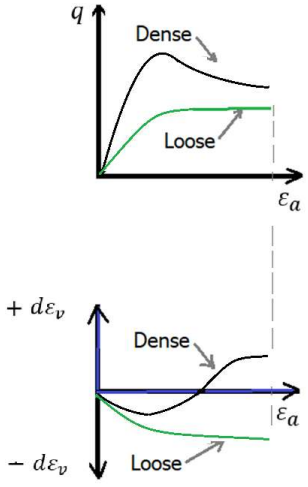

Figure 4: Stress-strain response of soil

1.8 SOIL YIELD SURFACE BASED ON THE CRITICAL STATE COCNCEPT

Effective confining stress (p), deviatoric stress (q), and void ratio (e) were among the crucial parameters utilized in the creation of critical

state models. With respect to cylindrical triaxial compression, those parameters are described below:

For the axissymmtery triaxial condition, $\boldsymbol{\sigma_1 = \sigma_2}$ and $\boldsymbol{\varepsilon_1 = \varepsilon_2}$; hence the work done on a test specimen per unit volume is given by

$$dW = \sigma_1 d\varepsilon_1 + \sigma_2 d\varepsilon_2 \quad (18)$$

$$dW = \left(\frac{\sigma_1 + 2\sigma_3}{3}\right)(d\varepsilon_1 + 2d\varepsilon_3) + (\sigma_1 - \sigma_3)\frac{2}{3}(d\varepsilon_1 - d\varepsilon_3) \quad (19)$$

Now let us define the above parameters as given below:

$$p = \frac{\sigma_1 + 2\sigma_3}{3} = \frac{J_1}{3}$$
$$= \text{mean effective stress}$$

Deviatoric stress of shear stress is given by;

$$q = \sigma_1 - \sigma_3 = \sqrt{2J_{2D}} \quad (20)$$

Volumetric incremental strain is given by;

$$d\varepsilon_v = d\varepsilon_1 + 2d\varepsilon_3 \quad (21)$$

Incremental shear strain is given by;

$$d\varepsilon_s = \frac{2}{3}(d\varepsilon_1 + d\varepsilon_3) \quad (22)$$

Therefore the quantitu dW can be written:

$$dW = pd\varepsilon_v + qd\varepsilon_s \quad (23)$$

The below figure shows typical results of undrained triaxial tests on NC samples. As it can be seen, the stress paths are geometrically similar and the ultimate states Q1, Q2, Q3, etc, lie on a straight line on the q-p plot. The same states are observed to lie on a curve which is similar to the isotropic consolidation line on e-p plot (Desai & Siriwardane, 1984).

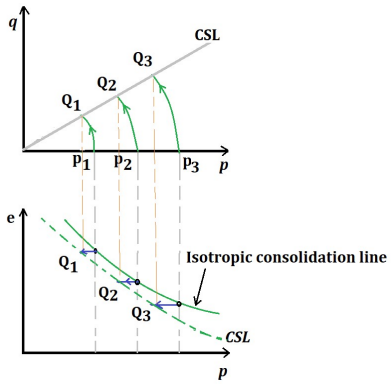

Figure 5: Undrained stress paths for normally consolidated clay

Typical results of stress paths in draned triaxial tests on NC clay sample are shown in Figure 6 as a function of deviatoric stress q, mean confining pressue p and void ratio.

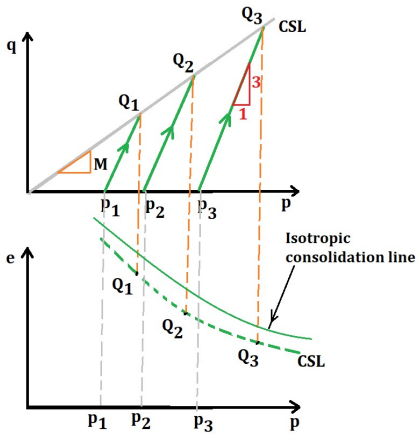

Figure 6: Drained stress paths for normally consolidated clay

Figure 6 demonstrates that, the ultimates states (failure points) also lie on the critical state (critical void ratio) line. The slope of the CSL on q-p plot is M and it is a material parameter. It is noted in Figure 5 and Figure 6 that material failure can happen when the material reaches the CSL.

1.9 STATE BOUNDARY SURFACE IN 3D SPACE OF DEVIATORIC STRESS-MEAN CONFINING PESSURE-VOID RATIO

Figure 7 shows a schematic representation of soil response as a function of sear stress q, confining stress p and void ratio e (Roscoe K. H., 1970; Roscoe, Schofield, & Wroth, 1958). Two surfaces ABCD and BCC'B' intersect at the CSL.

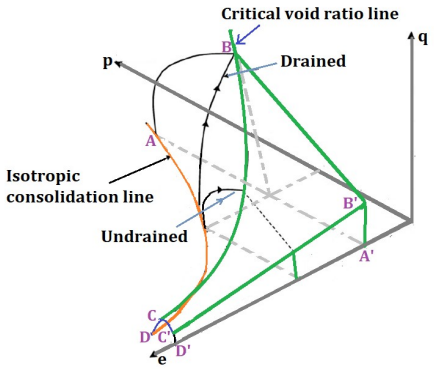

Figure 7: Isometric view of yeild surface

The material can undergo any state (q, p, e) below the two surfaces ABCD and BCC'B'. States of wet and isotropic normally consolidated (or loose) soil lie below the surface ABCD, whereas dry and overconsolidated (or dense) soil lie below BCC'B' surface. Before the material response reach CSL, it passes through states of yielding. The material hardens as it moves from one state of yileding to another. Subsequent yileding can lead to a state when the material is sheared without changing its volume. Figure 8 shows a projection of the crical void ratio line (or critical state line CSL) on the $q-p$ space and the yield surfaces. The projection of critical void ratio line (Figure 7) is usually a straight line passing through the origin of $q-p$ plot (Figure 8). The projection of the state boundary surface form continuous curves and are referred to as yield surface, yield locus or yield cap shown in Figure 8.

Figure 8 shows that point A is within the yield surface on $q-p$ space and it is a combination of q and p. The soil will respond elastically to the combination of q and p stresses when all possible combinations are contained within the yield surface (point A in Figure 8). On the initial yield surface, point B represents a novel combination of q and p. The yielding of steel rebar under tensile stresses is analogous to the yielding of the soil at point B. The current yield surface expands so that the stress point (q and p) lies on the expanded yield surface (points C and D) and not outside the expanded yield surface in the event that any stress point (of q and p) tends to fall outside the current yield surface passing through point B. The soil responds elastoplastically when there are effective stress paths that connect the B, C, and D points directly.

Spherical, bullet and elliptical shapes are assumed to be yield surfaces of soils. A yield surface intersects the CSL at the critical point. For NC clay, yield surfaces exist only between the CSL and p axis. Continuation of these surfaces from the CSL the origin of q-p space is shown in dashed lines (Figure 8) in order to indicate a complete shape of the yield locus. The mean confining pressure corresponding to the intersecton of the yield locus and the p -axis is denoted by p_0. Each surface has its unique p_0 which defines the strain hardening response.

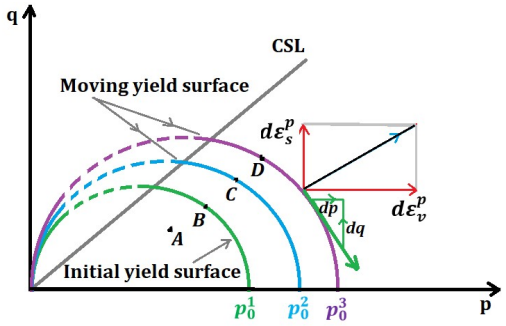

Figure 8: Yield locus in q-p space.

Soil response on $q-p$ plot is simulated by conventional triaxial tesst and that on $e-p$ space by one dimensional consolidation tests (Roscoe, Schofield, & Wroth, 1958). The numerical implementation of the MCC constitutive law within the framework of the critical state concept is the subject of the subsequent sections.

1.10 STRESS AND STRAIN PREDICTION BY THE MCC MODEL IN THREE DIMENSIONAL STATE OF STRESES

Let us consider the response of saturated clay to isotropic loading in $\boldsymbol{e-\ln(p)}$ plot as shown in Figure 9. Line AC is the virgin compression line while BD is the unloading line and DB is reloading line. Slope of AB is denoted by $\boldsymbol{\lambda}$ and slope of BD is denoted by $\boldsymbol{\kappa}$. Because of the elasto-plastic nature of soil response to the loading, the unloading path BD will not follow the AB loading line. Since the unloading path BD and reloading path DB are the same paths, they show elasic response (elastic incremental void ratio e^e). As shown in Figure 9, the vertical distance shows incremental plastic void ratio $\mathbf{e^p}$. Now, we can write change in void ratio during the loading-reloading cyclesas below:

$$\Delta e = e_A - e_B = \lambda(\boldsymbol{ln}p_B - \boldsymbol{ln}p_A) \quad (24)$$

$$\Delta e^e = e_D - e_B = \kappa(\boldsymbol{ln}p_B - \boldsymbol{ln}p_D) \quad (25)$$

$$\Delta e^p = \Delta e^t - \Delta e^e \quad (26)$$

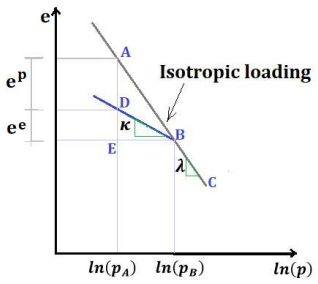

Figure 9: One dimensional consolidation response of OC clay on $\boldsymbol{e} - \mathbf{ln}(\boldsymbol{p})$ plot

Differentiating the above two relationships give us:

$$de = -\lambda \frac{dp}{p} \tag{27}$$

$$de^e = -\boldsymbol{\kappa} \frac{dp}{p} \tag{28}$$

$$de^p = de - de^e = -(\lambda - \boldsymbol{\kappa}) \frac{dp}{p} \tag{29}$$

where the superscript de^e denotes the recoverable incremental elastic void ratio and de^p is the irrecoverable plastic incremental void ratio. With compressive volumentric strain positive, we have;

$$d\varepsilon_v = -\frac{de}{1+e_0} = \frac{\lambda}{1+e_0}\frac{dp}{p} \tag{30}$$

Elastic component of the above volumetri strain is given by;

$$d\varepsilon_v^e = -\frac{de^e}{1+e_0} = \frac{\boldsymbol{\kappa}}{1+e_0}\frac{dp}{p} \tag{31}$$

According to the normality rule, incremental plastic strain vector $d\varepsilon_v^p$ is normal to the yield surface (Figure 8) at any point on the yield locus (Chen & Mizuno, 1990). Thus, ratio of the volumetric plastic strain vector $d\varepsilon_v^p$ to the plastic shear strain $d\varepsilon_s^p$ is given by;

$$\frac{d\varepsilon_v^p}{d\varepsilon_s^p} = -\frac{dp}{dq} \tag{32}$$

1.11 EQUATION OF THE YIELD LOCUS OF THE MCC MODEL

Let us define stress ratio

$$\eta = \frac{q}{p} \tag{33}$$

$$q = \eta p \tag{34}$$

$$dq = pd\eta + \eta dp \tag{35}$$

Slope of the yield curve at any point (p, q) on the yield surface (Figure 8) is given by;

$$\psi = -\frac{dq}{dp} \tag{36}$$

Substituting the value of ψ into equation (32), it is written

$$\frac{d\varepsilon_v^p}{d\varepsilon_s^p} = -\frac{dq}{dp} = -\psi \tag{37}$$

In equations (36) and (37), the sign of ψ is negative because, q decreases with an increment in p.

$$=> dq = -\psi dp \tag{38}$$

Substitution of equation (38) in to equation (35) results in the following expression;

$$pd\eta + \eta dp = -\psi dp \tag{39}$$

By rearranging, this can be written below (Desai & Siriwardane, 1984);

$$=> \frac{dp}{p} + \frac{d\eta}{\eta + \psi} = 0 \tag{40}$$

The above equation (40) defines a yield locus. Since all sucessive yield loci (hardening caps) are geometrically the same (Desai & Siriwardane, 1984), the slope of the hardening cap ψ is only a function of the stress ratio η. Therefore, an equation for the yield curve shown in Figure 8 is derived by integrating equation (40);

$$\int_{p_0}^{p} \frac{dp}{p} + \int_{0}^{\eta} \frac{d\eta}{\eta + \psi} = 0 \tag{41}$$

$$=> lnp - lnp_0 + \int_{0}^{\eta} \frac{d\eta}{\eta + \psi} = 0 \tag{42}$$

Equation (42) represents an yield curve which passes through a point $(p_0, 0)$ on p –axis; where p_0 is treated as the hardening parameter which is unique for any yield surface. Equation (42) canbe expressed in the following differential form:

$$\frac{dp}{p_0} - \frac{dp}{p} - \frac{d\eta}{\psi + \eta} = 0 \quad (43)$$

Inserting $p = p_0$ in equation (29), the following equation is written for incremental plastic void ratio;

$$de^p = -(\lambda - \boldsymbol{\kappa})\frac{dp_0}{p_0} \quad (44)$$

Substituting equation (43) into (44), it can be written;

$$de^p = -(\lambda - \boldsymbol{\kappa})\left(\frac{dp}{p} + \frac{d\eta}{\psi + \eta}\right) \quad (45)$$

Therefore, the plastic volumentric strain vector can be written:

$$d\varepsilon_v^p = \frac{de^p}{1+e} = \frac{\lambda - \kappa}{1+e}\left(\frac{dp}{p} + \frac{d\eta}{\psi + \eta}\right) \quad (46)$$

In the Cam-clay model it is assumed that

$$dW = Mpd\varepsilon_s \quad (47)$$

Using equation (23), it is written;

$$pd\varepsilon_v^p + qd\varepsilon_s^p = Mpd\varepsilon_s \quad (48)$$

Since there is no recoverable energy associated with shearing strain (Desai & Siriwardane, 1984),it is assumed that $\boldsymbol{d\varepsilon_s^e = 0}$. Substituting $\boldsymbol{d\varepsilon_s = d\varepsilon_s^p}$ into equation (48), it is writen;

$$\frac{d\varepsilon_s^p}{d\varepsilon_v^p} = \frac{1}{M - \eta} \quad (49)$$

Substituting equation (49) into equation (37), it is now written for the modified Cam-clay model,

$$\psi_c = M - \eta \quad (50)$$

In the above equation (50), the subscript $\boldsymbol{c}$ stands for the Cam-clay. In the MCC model the dissipated energy during plastic deformation is written:

$$dW = p\sqrt{\left(d\varepsilon_v^p\right)^2 + M^2\left(d\varepsilon_s^p\right)^2} \quad (51)$$

Using equations (47) to (51), it is written;

$$\frac{d\varepsilon_s^p}{d\varepsilon_v^p} = \frac{2\eta}{M^2 - \eta^2} \quad (52)$$

$$\psi_{cm} = \frac{M^2 - \eta^2}{2\eta} \quad (53)$$

where, the subscripts cm is used to idicate that the value of above ψ is for the MCC model.

Once ψ is substituted into equation (41) , the yield locus for the MCC model can be found by the integrations of equation (41);

$$\int_{p_0}^{p}\frac{dp}{p} = -\int_{0}^{\eta}\frac{d\eta}{\eta + \frac{M^2 - \eta^2}{2\eta}} \quad (54)$$

$$=> \ ln(M^2 + \eta^2) - ln(M^2) = -lnp + lnp_0 \quad (55)$$

$$M^2p^2 - M^2p_0p + q^2 = 0 \quad (56)$$

Equation (56) is the equation of an ellipse on $\boldsymbol{q}$ **-** $\boldsymbol{p}$ plot. From equation (30) and (46), it can be written that,

$$d\varepsilon_v^p = d\varepsilon_v - d\varepsilon_v^e = \left(\frac{\lambda - \kappa}{1 + e^0}\right)\frac{dp_0}{p_0} \quad (57)$$

$$=> \frac{\partial p_0}{\partial \varepsilon_v^p} = \frac{p_0(1 + e_0)}{\lambda - \kappa} \quad (58)$$

From equation (56), the yield function is expressed below;

$$f = M^2p^2 - M^2p_0p + q^2 = 0 \quad (59)$$

where, q is expressed in terms of 3D triaxial state of stresses

$$q = \sigma_1 - \sigma_3 \quad (60)$$

Stress invariants are introduced in the equation of yield surface f when 3D incremental plasticity computation is performed.

$$q = \sqrt{3J_{2D}} \quad (61)$$

where , $J_{2D} = \frac{1}{6}[(\sigma_{11} - \sigma_{22})^2 + (\sigma_{22} - \sigma_{33})^2 + (\sigma_{11} - \sigma_{33})^2] + \sigma_{12}^2 + \sigma_{23}^2 + \sigma_{31}^2$

The yield function can be written in terms of the stress invariants (Chen & Mizuno, 1990);

$$f = M^2 I_1^2 - M^2 I_1 I_{10} + 27 J_{2D} = 0 \quad (62)$$

where, $I_1 = 3p = (\sigma_{11} + \sigma_{22} + \sigma_{33})$ and I_{10} is the value of I_1 at the intersection of the yield surface with the I_1axis which is analogous to p_0 axis. The parameter I_{10} is a hardening paramter which depends on the plastic volumetric strain (Chen & Mizuno, 1990).

When soil yields, the stress point will be on the yield surface. It is expressed by;

$$f = f\left(p, q, p_0\left(\varepsilon_v^p\right)\right) \quad (63)$$

$$df = \frac{\partial f}{\partial q} dq + \frac{\partial f}{\partial p} dp + \frac{\partial f}{\partial \varepsilon_v^p} d\varepsilon_v^p = 0 \quad (64)$$

The normality rule for plastic deformation can be written as;

$$d\varepsilon_{ij}^p = \overline{d\lambda} \frac{\partial Q}{\partial \sigma_{ij}} \quad (65)$$

where, Q is the plastic potential and $\overline{d\lambda}$ is the scalar parameter of proportionality

$$d\varepsilon_{ij}^p = \overline{d\lambda} A_{ij} \quad (66)$$

$$A_{ij} = \frac{\partial Q}{\partial \sigma_{ij}} = \frac{\partial Q}{\partial p}\left(\frac{\partial p}{\partial \sigma_{ij}}\right) + \frac{\partial Q}{\partial q}\left(\frac{\partial q}{\partial \sigma_{ij}}\right) \quad (67)$$

From equation (66), plastic volumetric strain

$$d\varepsilon_v^p = d\varepsilon_{ii}^p = \overline{d\lambda} A_{ii} \quad (68)$$

Let us define

$$B_{ij} = \frac{\partial f}{\partial \sigma_{ij}} = \frac{\partial f}{\partial p}\left(\frac{\partial p}{\partial \sigma_{ij}}\right) + \frac{\partial f}{\partial q}\left(\frac{\partial q}{\partial \sigma_{ij}}\right) \quad (69)$$

Now, quation (64) gives us;

$$df = B_{ij} d\sigma_{ij} + \frac{\partial f}{\partial \varepsilon_v^p} d\varepsilon_v^p = 0 \quad (70)$$

The total strain increments are assumed to be the vector sum of the elastic and plastic strain increments. Using tensor algebra, it can be written;

$$d\varepsilon_{ij}^e = d\varepsilon_{ij} - d\varepsilon_{ij}^p \quad (71)$$

Using Hook's law, we can write;

$$d\sigma_{ij} = C_{ijkl}\left(d\varepsilon_{kl} - d\varepsilon_{kl}^p\right) \quad (72)$$

Now, we can get from equations (68) and (70);

$$df = B_{ij} C_{ijkl}\left(d\varepsilon_{kl} - \bar{\lambda} A_{kl}\right) + \frac{\partial f}{\partial \varepsilon_v^p} \overline{d\lambda} A_{ii} = 0 \quad (73)$$

Where the value of $\overline{d\lambda}$ is given by;

$$\overline{d\lambda} = \frac{B_{ij} C_{ijkl} d\varepsilon_{kl}}{B_{ij} C_{ijkl} A_{kl} - \frac{\partial f}{\partial \varepsilon_v^p} A_{ii}} \quad (74)$$

Now, the constitutive elastoplastic relation can be expressed in tensor format (Desai & Siriwardane, 1984);

$$d\sigma_{ij} = C_{ijkl} d\varepsilon_{kl} - \frac{C_{ijkl} A_{kl} B_{mn} C_{mnrs} d\varepsilon_{rs}}{B_{mn} C_{mnrs} A_{rs} - \frac{\partial f}{\partial \varepsilon_v^p} A_{ii}} \quad (75)$$

$$\Rightarrow d\sigma_{ij} = \left[C_{ijrs} - \frac{C_{ijkl} A_{kl} B_{mn} C_{mnrs}}{B_{mn} C_{mnrs} A_{rs} - \frac{\partial f}{\partial \varepsilon_v^p} A_{ii}}\right] d\varepsilon_{rs} \quad (76)$$

The constitutive relation presented by equation (76) is in tensor fomrat. It can be exprssed in matrix format and solved by GET.

$$\{d\sigma\} = [C^{ep}]\{d\varepsilon\} \quad (77)$$

Where C^{ep} is the elastoplastic constitutive matrix. It can be calculated using the equation;

$$[C^{ep}] = [C^e] - [C^p] \quad (78)$$

For associative flow rule, it is written;

$$\frac{\partial Q}{\partial \sigma_{ij}} = \frac{\partial f}{\partial \sigma_{ij}} \quad (79)$$

$$\Rightarrow A_{ij} = B_{ij} \quad (80)$$

Equation (80) can be written in terms of invariants;

$$A_{ij} = \frac{\partial f}{\partial I_1}\frac{\partial I_1}{\partial \sigma_{ij}} + \frac{\partial f}{\partial J_{2D}}\frac{\partial J_{2D}}{\partial \sigma_{ij}} \quad (81)$$

Differentiating equation (81) gives us;

$$A_{ij} = M^2(2I_1 - I_{10})\delta_{ij} + 27S_{ij} \quad (82)$$

where, the deviatoric stress tensor;

$$S_{ij} = \frac{\partial J_{2D}}{\partial \sigma_{ij}} = \sigma_{ij} - \frac{I_1}{3}\delta_{ij} \quad (83)$$

Now, using the chain rule of differentiation, we have

$$\frac{\partial f}{\partial \varepsilon_v^p} = \frac{\partial f}{\partial p_0}\frac{\partial p_0}{\partial \varepsilon_v^p} = -\frac{M^2 p p_0(1+e_0)}{\lambda - \kappa} \quad (84)$$

$$\frac{\partial f}{\partial \varepsilon_v^p} = -\frac{M^2 I_1 I_{10}(1+e_0)}{\lambda - \kappa} \quad (85)$$

Using equations (58), (68) and (81), we can get;

$$dI_{10} = \frac{I_{10}(1+e_0)}{\lambda - \kappa}\bar{\lambda}A_{ii} \quad (86)$$

2. THE MCC MODEL IMPLEMENTATION IN THE ISU METHOD

Our aim here is to determine the stress increment $d\sigma_{ij} = [d\sigma_{11}, d\sigma_{22}d\sigma_{33}, 0,0,0]$ at a point in clay soil corresponding to a given strain increment, i.e., $d\varepsilon_{ij} = [d\varepsilon_{11}, d\varepsilon_{22}d\varepsilon_{33}, 0,0,0]$ under isotropic triaxial strain condition. Stress increments are calculated from equation (76) using Gauss elimination technique (GET). A schematic flow chart for implementation of the MCC model using the GET is shown in Figure *10*. The model in the chapter is implemented in the ISU method. The C++ computer programming performed for implementation of the model is listed in Appendix.

2.1 INPUT PARAMETERS FOR THE MCC MODEL IMPLEMENTATION IN THE ISU METHOD

Following parameters were declared in the appendix with the C++ code for numerical implementation of the modified Cam clay.

1. **Calculation type**:

ISU and GET were employed.

2. **Material Type**:
Clay soil

3. **Yield status**:

Isotropic hardening, i.e., the yield surface expands uniformly without changing its position in the stress space.

4. **Material constants**:
EG=Bulk shear modulus
EK=Elastic bulk modulus
Lamda = slope of normal consolidation line (NCL)
M = slope of critical state line (CSL)
Kappa= slope of swelling line
I_{10} = Hardening parameter, i.e., size of the yield surface
e_0 = initial void ratio

5. **Strain increments**,

$$DE = d\varepsilon_{ij} = [d\varepsilon_{11}, d\varepsilon_{22}, d\varepsilon_{33}, 0,0,0]$$

6. **Stress state at previous step**;

$$S = \sigma_{ij}^n = [\sigma_{11}, \sigma_{22}, \sigma_{33}, 0,0,0]$$

2.2 ALGORITHM FOR IMPLEMENTATION OF THE MCC MODEL

Here, this thesis paper will outline step by step procedure with a view to implement the MCC model by incremental stress update method. A self-teaching flow chart in Figure *10* is used to do the computer coding.

Step 1: Take input quantities EG, EK, M, Lamda, Kappa, I10, e_0 , σ_{ij}^n, $d\varepsilon_{ij}$ for strain controlled simulation, $d\sigma_{ij}$ for stress controlled simulation.

Step 2: Compute C^e

Step 3. Compute $d\sigma_{ij} = C^e d\varepsilon_{ij}$ if all six components of $d\varepsilon_{ij}$ are known. But is all components of $d\sigma_{ij}$ are known, compute $d\varepsilon_{ij}$ by solving $d\sigma_{ij} = C^e d\varepsilon_{ij}$ with the application of GET.

Step 4: Compute trial stress $\sigma_{ij}^t = \sigma_{ij}^n + d\sigma_{ij}$

Step 5: Compute yield function f of the MCC model

Step 6: If $f < 0$, final stress state will be $\sigma_{ij}^{n+1} = \sigma_{ij}^t$ and go to step 8

Else $f > 0$; elasto-plastic computation is to be performed

Step 7 (a): Compute $\frac{\partial f}{\partial \sigma_{ij}}$ as given by equation (82)

Step 7(b) compute $\frac{\partial f}{\partial \sigma_{ii}}$

Step 7(c): compute $\frac{\partial f}{\partial \varepsilon_v^p}$ as given by equation (85)

Step 7(d): Compute $C_{ijkl}\frac{\partial f}{\partial \sigma_{ij}}$

Step 7(e): Compute $\frac{\partial f}{\partial \sigma_{mn}} C_{mnrs} \frac{\partial f}{\partial \sigma_{rs}}$

Step 7(f): compute $\frac{\partial f}{\partial \varepsilon_v^p}$ as given by equation (85)
Step 7(g): compute C^{ep} as given by equation (76)
Step 7(h): compute $d\sigma_{ij}^{ep} = C^{ep} d\varepsilon_{ij}$
Step 7(i): compute $\bar{\lambda}$
Step 7(j): Compute $d\varepsilon_v^p$ as given by equation (68)
Step 7(k): Update hardening parameter as given by equation (86)
Step 7(l): Update void ratio parameter as given by equation (30)
Step 8: Compute: σ_{ij}^{n+1},

ε_{ij}^{n+1}

q= deviatoric stress
ε_v = volumetric strain
shear strain, $\gamma = \varepsilon_3 - \varepsilon_1$
Step 9: Go to step 8 to generate more solutions of stresses and strains to plot stress-strain curve.

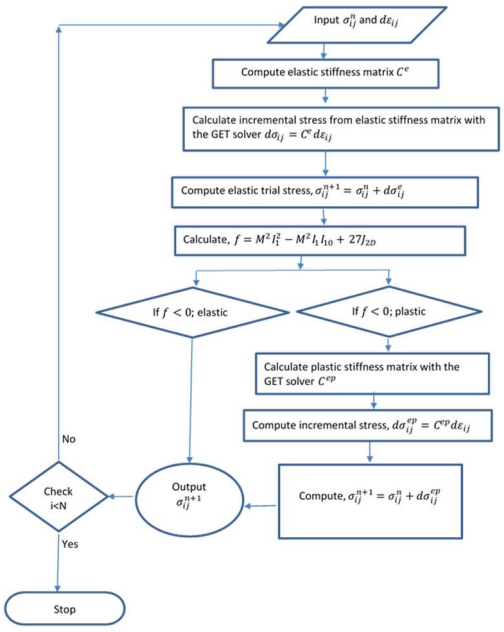

Figure 10: Flow chart for implementation of *the MCC model by incremental stress update method.*

2.4 INTERNAL VARIABLES DECLARED IN THE VISUAL C++ PROGRAM PROVIDED IN APPENDIX FOR THE ISU PROCEDURE IMPLEMENTATION

S1 = Elastic trial stress
LC = Loading condition
D1 = increment vector according to loading condition
DIJ = Kronecker delta=$\delta_{ij} = [1,1,1,0,0,0]$
DS = incremental stress = $d\sigma_{ij} = [d\sigma_{11}, d\sigma_{22} d\sigma_{33}, 0,0,0]$
I1 = First invariant of stress tensor = $\sigma_{ii} = (\sigma_{11} + \sigma_{22} + \sigma_{33})$
SD = deviatoric stress tensor = $\sigma_{ij} - \frac{1}{3} I_1 \delta_{ij}$
DFDS = Normal vector to the yield surface = $\frac{\partial Q}{\partial \sigma_{ij}} = \frac{\partial f}{\partial \sigma_{ij}}$
EM=elastic matrix= C^e
EPM = Elastoplastic matrix = C^{ep}
EMN = $C_{ijkl} \frac{\partial f}{\partial \sigma_{kl}}$
TRNEMN = $\frac{\partial f}{\partial \sigma_{mn}} C_{mnrs} \frac{\partial f}{\partial \sigma_{rs}}$
J2=second invariant of deviatoric stress tensor
DLAMDA = scalar multiplier = $\bar{\lambda}$ is defined by equation (74)
DFDEPv = $\frac{\partial f}{\partial \varepsilon_v^p}$
DEPv = $\overline{d\lambda} \frac{\partial f}{\partial \sigma_{ii}}$
Ev = volumetric strain
Es = axial strain
q = deviatoric stress = $\sqrt{3J_2}$
p= mean effective stress $p = \frac{I_1}{3}$
gamma = shear strain =$\varepsilon_3 - \varepsilon_1$
E = total strain
ε_v = volumetric strain = $\varepsilon_1 + \varepsilon_2 + \varepsilon_3$

2.5 VERIFICATION OF THE CALCULATED RESPONSE OBTAINED FROM THE ISU PROCEDURE

In the following, numerical experiments are carried out to demonstrate the performance of the ISU solution of the MCC model response. It shows the behavior of NC and OC clay in both drained and undrained isotropic triaxial compression tests. Strain controlled analyses were used in the drained and undrained compression tests. Axial and radial strain increments were input to compute stress and volumetric strain increments. Strain controlled test were used for numerical triaxial tests on NC and OC clay materials because instability occurred when strain softening took place in stress-controlled computation.

2.6 NUMERICAL TRIAXIAL TEST ON NC CLAY IN DRAINED CONDITION

In the first instance of the numerical triaxial test, the clay sample was normally consolidated in the initial isotropic pressure $\sigma_{11} = \sigma_{22} = \sigma_{33} = 200$ kPa (Figure *11*). It is assumed that the pore pressures remain equal to zero during the consolidation process. The sample is then sheared in drained conditions up to failure. Strain controlled shearing process was

implemented as the following: $\varepsilon_{11} = \varepsilon_{22} = 0;\ \varepsilon_{33} = 0.0001; \varepsilon_{12} = \varepsilon_{23} = \varepsilon_{31} = 0.$.
For numerical prediction of the behavior of NC clay under drained isotropic compression (triaxial CD test) test by the DR technique, the material properties used by the Visual C++ code given in *Table 1*. The input data were obtained from Chapter 11 of the geotechnical text book (Budhu, 2011).

Table 1: Input loading and boundary conditions used to model the stress-strain response of NC clay in drained triaxial compression test.

Material properties	Values
Soil Poisson ratio	0.3
Elastic bulk modulus, EK	10976 kPa
Bulk shear modulus, EG	4221 kPa
slope of CSL, M	0.95
slope of NCL, $\boldsymbol{\lambda}$	0.25
slope of swelling line, $\boldsymbol{\kappa}$	0.05
Initial void ratio, $\boldsymbol{e_0}$	1.15
Hardening parameter, $\boldsymbol{I_{10}}$	600 kPa
Initial stress, $\boldsymbol{\sigma_{ij}^n}$	[200, 200, 200, 0, 0, 0]
Initial strain increment, $\boldsymbol{d\varepsilon_{ij}}$	[0, 0, 0.0001, 0, 0, 0]

Stress-strain behavior predicted from the C++ coomputer program of the FE method are shown in Figure *11*. Negative volumetric strains indicate contraction of the soil mass. The ISU solutions for the soil response in numerical CD triaxial are compared with the analytical solutions presented in (Budhu, 2011). Using the soil properties *Table 1*, numerical triaxial drained test on NC clay soil was conducted in Finite Element simulation of the software PLAXIS (PLAXIS, 2016). In Figure *11*, the PLAXIS simulation results are compared with the stress-strain and stress response calculated from the ISU method and analytical method.

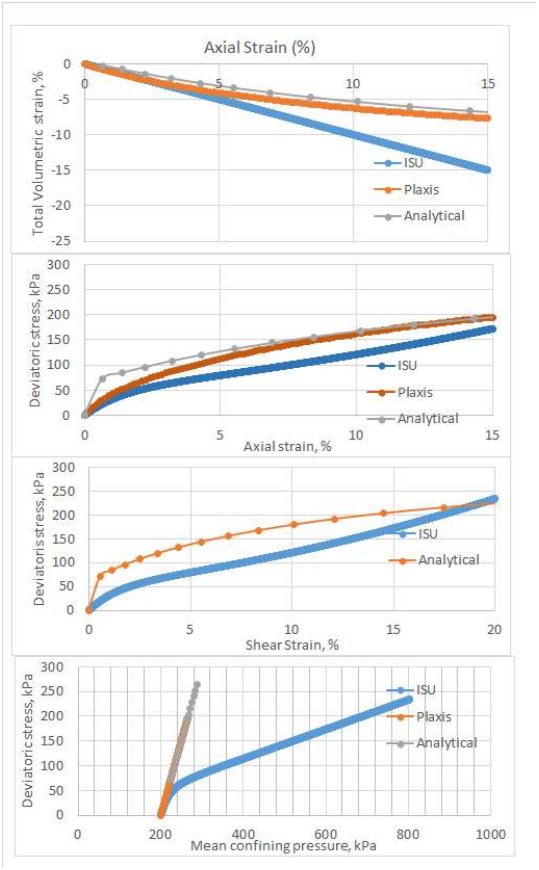

Figure 11: Numerical prediction of the behavior of NC clay in drained isotropic compression test by the ISU technique.

2.7 NUMERICAL TRIAXIAL TEST ON NC CLAY IN UNDRAINED CONDITION

In the first instance, the clay sample is normally consolidated under the initial isotropic pressure pressure $\boldsymbol{\sigma_{11} = \sigma_{22} = \sigma_{33} = 200}$ kPa(Figure 12). It is assumed that the pore pressures remains equal to zero during the consolidation process. The sample is then sheared in undrained conditions up to failure, when total elasto-plastc volume of the soil element remains equal to zero. This is implemented as the following condition: $\boldsymbol{\varepsilon_{11} = \varepsilon_{22} = -0.0005;\ \varepsilon_{33} = 0.001; \varepsilon_{12} = \varepsilon_{23} = \varepsilon_{31} = 0}$. Material properties used in the ISU method are listed in below Table 2.

Table 2: Input loading and boundary conditions used to model the stress-strain response of NC clay in undrained triaxial compression test.

Clay soil properties	Values
Soil Poisson's ratio	0.3
Elastic bulk modulus, EK	10976 kPa
Bulk shear modulus, EG	4221 kPa
Slope of CSL, M	0.95

Slope of NCL, λ	0.25
Slope of swelling line, κ	0.05
Initial void ratio, e_0	1.15
Hardening parameter, I_{10}	600 kPa
Initial isotropic stress components, σ_{ij}^{n}	[200, 200, 200, 0, 0, 0], KPa
Initial strain increment, $d\varepsilon_{ij}$	[-0.0005, -0.0005, 0.001, 0, 0, 0]

Stress-strain response predicted from the C++ code of the ISU method are shown in Figure 12. Using the soil properties ISU method are listed in below Table 2.

Table 2, numerical triaxial undrained test on NC clay soil was conducted in Finite Element simulation of the software PLAXIS (PLAXIS, 2016). In Figure 12: Response of NC clay in undrained isotropic compression test by the ISU method. Figure 12, the PLAXIS simulation results are compared with the stress-strain and stress response calculated from the ISU method and analytical method.

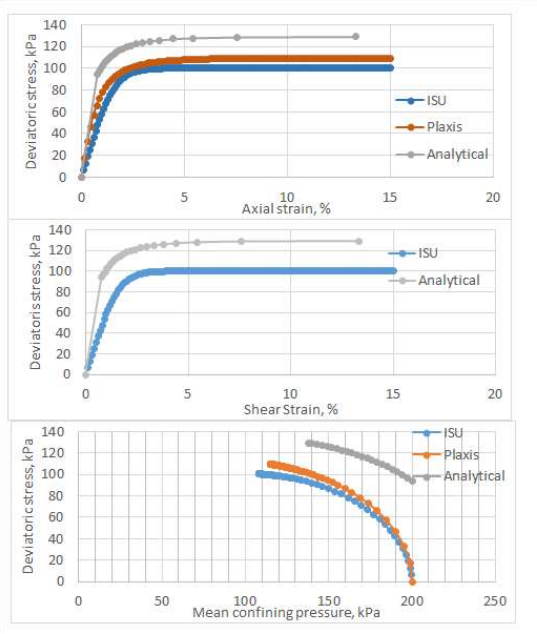

Figure 12: Response of NC clay in **undrained** isotropic compression test by the ISU method.

2.8 DISCUSSION OF NC SOIL RESPONSE CALCULATED USING ISU SIMULATION, PLAXIS SIMULATION, AND ANALYTICAL METHOD

The MCC model was numerically implemented by ISU simulation, PLAXIS simulation, and Analytical method. Stresses and strains in the soil element noted from the computed results for NC drained clay are summarized in Table 3.

Table 3: Analytical method, PLAXIS Triaxial test simulation and ISU simulation comparison for NC soil in drained condition.

Soil response curve **Figure 11**	**Prediction by analytical method**	**Prediction by ISU method**	**Prediction by PLAXIS FE simulation**
Volumetric strain versus Axial strain	7% volume contraction at 15% axial strain	15% volume contraction at 15% axial strain	7.5% volume contraction at 15 % axial strain
q versus γ (deviatoric stress versus axial strain)	Ultimate Deviatoric stress = 200 kPa at 15% axial strain,	Ultimate Deviatoric stress = 175 kPa at 15 % axial strain	Ultimate Deviatoric stress = 200 kPa at % axial strain
q versus γ (deviatoric stress versus shear strain)	Ultimate deviatoric stress capacity = 227 kPa at 20 % shear strain	Ultimate deviatoric stress capacity = 234 kPa is also at 20 % shear strain	Not calculated
q versus p (stress path)	Ultimate Deviatoric stress = 280 kPa at mean effective confining stress = 260 kPa	Ultimate Deviatoric stress = 234 kPa at mean effective confining stress = 803 kPa	Ultimate Deviatoric stress = 195 kPa at mean effective confining stress = 265 kPa

From Figure *11*, it is noted that the ISU wants to follow the PLAXIS and analytical solution of stress strain behavior as fast possible. This happens because plastic slope of the ISU solution curve has steep slope. It is evident that after a large number of increments in strain, the approximate solution from the ISU method diverges from analytical solution. It is noted from the slope (dq/dp) of the drained stress path (q versus p) shown in Figure *11* that the analytical solution reaches the CSL faster than FE solution and analytical method.

It is noted in Figure 12 that, deviatoric stress versus axial strain relation computed by the ISU method compares well with the analytical and PLAXIS results for NC clay in undrained numerical triaxial test. The numerical stress and strain response of the NC clay in undrained condition are summarized in Table 4.

Table 4: Analytical method, PLAXIS Triaxial test simulation and ISU simulation comparison for NC soil in undrained condition.

Soil response curve **Figure 12**	**Prediction by analytical method**	**Prediction by ISU method**	**Prediction by PLAXIS FE simulation**
q versus γ (deviatoric stress versus axial strain)	Ultimate Deviatoric stress = 135 kPa at 12.5% axial strain,	Ultimate Deviatoric stress = 100 kPa at 10 % axial strain	Ultimate Deviatoric stress = 110 kPa at 10 axial strain
q versus γ (deviatoric stress versus shear strain)	Ultimate deviatoric stress capacity = 130 kPa at 12.5 % shear strain	Ultimate deviatoric stress capacity = 100 kPa is also at 12.5 % shear strain	Not calculated
q versus p (stress path)	Ultimate Deviatoric stress = 130 kPa at mean effective confining stress = 143 kPa	Ultimate Deviatoric stress = 100 kPa at mean effective confining stress = 110 kPa	Ultimate Deviatoric stress = 110 kPa at mean effective confining stress = 120 kPa

The stress path in Figure 12 shows that the mean confining stress decreases from 200 kPa to 143 kPa, 110 kPa, and 120 kPa in analytical, ISU and PLAXIS analysis, respectively. This happens due to increase in excess pore water pressure in the saturated consolidated soil during deviatoric load application. The stress paths computed from the ISU and PLAXIS triaxial undrained tests compare very well. In all three approach of numerical tests: analytical, ISU and PLAXIS methods, the deviatoric stress is reduced relative to the drained case (Figure *11*). The stress path in Figure 12 shows a typical undrained response that reaches to the CSL line after moving away from the drained path shown in Figure *11*.

The implemented C++ computer program algorithm simulated both drained and undrained triaxial compression tests under the strain controlled conditions. The implemented ISU method employs back substitution of the Gaussian elimination technique to determine stress increments from a linear system of equations in a finite number of steps. The elasto-plastic stiffness matrix which connects stress and strain increments within this linear system of equations was updated at the beginning of each strain increment. Due to the large number of strain increments, the numerical ISU solution began to diverge from the analytical closed form solutions in the undrained case. In contrast, the PLAXIS solution utilizes an iterative convergence criterion to achieve the analytical solution.

CONCLUSION

The MCC numerical prediction of the stress-strain behavior of the NC and OC soil was implemented in the ISU approach. The MCC plasticity model's stress-strain equations were solved using the GET in the ISU method. Analytical solution and predicted stress-strain behavior of NC in both drained and undrained triaxially consolidated soil were compared. There was a satisfactory level of agreement between the analytical and numerical solutions. Elasto-plastic stiffness in linear stress update procedure of the ISU method are not as effcient as the PLAXIS FE simulation. Stress-strain response computed from the ISU method diverges from the analytical response of soil due to the rapid linear approximation of the soil stiffness in the plastic zone.

The hard reality is that, due to a lack of financing for scientific study, many geotechnical stress-strain problems that arise in the real world frequently remain unsolved in our scientific labs. It is feasible to predict with a high degree of precision how the clay soil will respond to both static and dynamic loads using numerical modeling. Such modeling requires understanding of mathematics and computer programming ability (Wood, 1991). Therefore, this study encourages future geotechnical engineers to use their knowledge of coding to simulate the response of geomaterials to various boundary and loading conditions.

DECLARATION OF COMPETING INTEREST

The author declare that he has no known competing financial interests or personal relationships that could have appeared to influence the work reported in this paper.

REFERENCES

[1] Borja, R. I. (1991). Cam-Clay plasticity, Part II: Implicit integration of constitutive equation based on a nonlinear elastic stress predictor. Computer Methods in Applied Mechanics and Engineering, 225-240. Retrieved from https://doi.org/10.1016/0045-7825(91)90256-6.

[2] Budhu, M. (2011). Soil Mehcanics and Foundations. John Wiley & Sons, Inc.

[3] Cassel, A. C., Kinsey, P. J., & Sefton, D. J. (1968). Cylindrical shell analysis by Dynamic Relaxation. Proceedings of the Institution of Civil Engineers, 75-84. doi:https://doi.org/10.1680/iicep.1968.8109

[4] Chen, W. F., & Mizuno, E. (1990). Nonlinear Analysis in Soil Mechanics: Theory and Implementation. Elsevier Science.

[5] Desai, C. S., & Siriwardane, J. H. (1984). Constitutive laws for engineering materials: With emphasis on geologic materials. New Jersey 07632: Prentice-Hall, Inc., Englewood Cliffs. Retrieved from https://doi.org/10.1002/nag.1610080310

[6] Hashiguchi, K., Saitoh, K., & Okayasu, T. (2002). Evaluation of typical conventional and unconventional plasticity models for prediction of softening behaviour of soils. Geotechnique 52 (8), 561-578, 561-578. doi:https://doi.org/10.1680/geot.2002.52.8.561

[7] Irons, B., & Ahmad, S. (1984). Techniques of Finite Elements. the University of Michigan.

[8] Lambe, T. W., & Whitman, R. V. (1969). Soil Mechanics. Wiley.

[9] Ortiz, M., & Martin, J. B. (1989). Symmetry-preserving return mapping algorithms and incrementally extremal paths: A unification of concepts. International Journal for Numerical Methods in Engineering, 1839-1853. doi:10.1002/nme.1620280810

[10] Otter, J. R. (1966). Dynamic relaxation compared with other iterative finite difference methods. Nuclear Engineering and Design, 183-185. doi:https://doi.org/10.1016/0029-5493(66)90157-9

[11] PLAXIS. (2016). PLAXIS Reference Manual. Bentley Systems Inc.

[12] Riks, E. (1979). An incremental approach to the solution of snapping and buckling problems. International Journal of Solids and Structures, 529-551. doi:https://doi.org/10.1016/0020-7683(79)90081-7

[13] Roscoe, K. H. (1970). The Influence of Strains in Soil Mechanics. Géotechnique. Retrieved from https://doi.org/10.1680/geot.1970.20.2.129

[14] Roscoe, K. H., Schofield, A. N., & Wroth, C. P. (1958). On the Yielding of Soils. Géotechnique, 22-53. doi:http://doi.org/10.1680/geot.1958.8.1.22

[15] Siddiquee, M. S., Tanaka, T., & Tatsuoka, F. (1995). Tracing the equilibrium path by dynamic relaxation in materially nonlinear problems. International journal for numerical and analytical methods. doi:https://doi.org/10.1002/nag.1610191102

[16] Simo, J. C., & Taylor, R. (1986). A return mapping algorithm for plane stress elastoplasticit. https://doi.org/10.1002/nme.1620220310. doi:https://doi.org/10.1002/nme.1620220310

[17] Wood, d. M. (1991). Soil Behaviour and Critical State Soil Mechanics. Cambridge University Press. doi:https://doi.org/10.1017/CBO9781139878272

[18] Zienkiewicz, O. C., Taylor, R. L., & Zhu, J. Z. (2013). The Finite Element Method: Its Basis and Fundamentals. Elsevier Ltd. Retrieved from https://doi.org/10.1016/C2009-0-24909-9

APPENDIX

The C++ computer program is presented for the ISU method for numerical triaxial test simulation of the MCC model.

// C++ programming for source code for implementing the MCC model in the ISU method

```
#include<iostream>
#include<math.h>
#include<fstream>
int main()
{double S[6],S1[6],E[6],LC[6],DI[6];
double DIJ[6],DS[6],DE[6],SD[6],DEPv;
double DFDS[6],EM[6][6],EPM[6][6],EMN[6];
double TRNEMN,LAMDA,KAPPA;
double p,q,I1o,DLAMDA,e,M,Aii,I1,J2,gama,f;
double DFDEPv;
double EK,EG,EM1,EM2,EM3;
double y;
int i,j,k,n,count=0;
  //The variable 'gama' keeps the values of shear strain and prints
  them in the gama.text file. The //variable 'pout' keeps the values
  of mean effective stress p and prints the in the pout.txt file. The
  //variable 'qout' keeps the values of q and prints them in them
  qout.txt file. The variable Evout keeps //the values of volumetric
  strain and prints them in Evout.txt file. The variable Eaout keeps
  the values //of axial strain and prints them in Eaout.txt file.
std::ofstream gamaout("gama.txt");
std::ofstream pout("p.txt");
std::ofstream qout("q.txt");
std::ofstream Evout("Ev.txt");
std::ofstream Eaout("Ea.txt");
EG=4221,EK=10976,M=0.95,LAMDA=.25,KAPPA=.05,e=1.15,I1o
=600;
// Cell pressures: sigma2, sigma2, sigma3
   for(i=0;i<6;i++){
      if(i<3)S[i]=200;
      else S[i]=.0;
   }
   for (i=0;i<=6;i++)
      E[i]=.0; DIJ[0]=1; DIJ[1]=1; DIJ[2]=1; DIJ[3]=0;
      DIJ[4]=0; DIJ[5]=0;
      do{
         EM1=EK+4/3*EG;
         EM2=EK-2/3*EG;
         EM3=EG;
         for(i=0;i<6;i++)
            for(j=0;j<6;j++) EM[i][j]=0;
            EM[0][0]=EM[1][1]=EM[2][2]=EM1;
            EM[3][3]=EM[4][4]=EM[5][5]=EM3;

EM[0][1]=EM[0][2]=EM[1][0]=EM[1][2]=EM[2][0]=EM[2][1]=EM2;
  //Appropriate loading condition LC and corresponding increment
  DI is given. // This listing of the ISU method simulates isotropic
  consolidated undrained (CIU) test where change in //volumetric
  strain is zero. LC=1.0 means strain increment is provided and
  LC=0.0 means stress //increment must be provided.
            LC[0]=1;DI[0]=0;
            LC[1]=1;DI[1]=0;
            LC[2]=1;DI[2]=0.0001;
            LC[3]=0;DI[3]=0;
            LC[4]=0;DI[4]=0;
            LC[5]=0;DI[5]=0;
                  for(i=0;i<6;i++){
            if(LC[i]==0){
                  DS[i]=DI[i];
                  DE[i]=0;
            }
            else {
                  DS[i]=0;
                  DE[i]=DI[i];
            }
         }
         for(i=0;i<6;i++){
               if(LC[i]==1){
                     for(j=0;j<6;j++)
                           if(LC[j]==0)DS[j]-=EM[i][j]*DE[i];
               }
         }
         for(k=0;k<5;k++){
               if(LC[k]==0){
                     for(i=k+1;i<6;i++){
                           if(LC[i]==0){
                                 y=EM[i][k]/EM[k][k];
                                 for(j=k;j<6;j++)
                                       if(LC[j]==0)EM[i][j]-=y*EM[k][j];
                           }
                     }
               }
         }

         for(i=0;i<6;i++)
               if(LC[i]==0)n=i;
               DE[n]=DS[n]/EM[n][n];
               for(i=n-1;i>=0;i--){
                     if(LC[i]==0){
                           y=DS[i];
                           for(j=i+1;j<=n;j++)
                                 if(LC[j]==0)y-=EM[i][j]*DE[j];
                                 DE[i]=y/EM[i][i];
                     }
               }
               for(i=0;i<6;i++){
                     if(LC[i]==1){
                           DS[i]=0;
                           for(j=0;j<6;j++)DS[i]+=EM[i][j]*DE[j];
                     }
               }
               for(i=0;i<6;i++)
                     if(LC[i]==0) DS[i]=DI[i];
                     for(i=0;i<6;i++)
                           S1[i]=S[i]+DS[i];
                     for(i=0;i<6;i++)
std::cout<<"S1["<<i+1<<"]::"<<S1[i]<<std::endl;
                  I1=(S1[0]+S1[1]+S1[2]);
                  for(i=0;i<6;i++)
                        SD[i]=S1[i]-(I1*DIJ[i])/3;
                        J2=(((S1[0]-S1[1])*(S1[0]-S1[1])+(S1[1]-
S1[2])*(S1[1]-S1[2])+(S1[2]-S1[0])*(S1[2]-
S1[0]))/6)+S1[3]*S1[3]+S1[4]*S1[4]+S1[5]*S1[5];
                        f=M*M*I1*I1-M*M*I1*I1o+27*J2;
                        if(f>0){
                              std::cout<<"It is now Elasto-plastic
state"<<std::endl;
                              EM1=EK+4/3*EG;
                              EM2=EK-2/3*EG;
                              EM3=EG;
                              for(i=0;i<6;i++)
                              for(j=0;j<6;j++) EM[i][j]=0;
                              EM[0][0]=EM[1][1]=EM[2][2]=EM1;
EM[3][3]=EM[4][4]=EM[5][5]=EM3;
EM[0][1]=EM[0][2]=EM[1][0]=EM[1][2]=EM[2][0]=EM[2][1]=EM2;
                              for(i=0;i<6;i++)
                              DFDS[i]=M*M*(2*I1-
I1o)*DIJ[i]+27*SD[i];
Aii=(DFDS[0]+DFDS[1]+DFDS[2]);
                              TRNEMN=0;
                              for(i=0;i<6;i++){
                                    EMN[i]=0;
                                    for(j=0;j<6;j++)
EMN[i]+=EM[i][j]*DFDS[j];
TRNEMN+=EMN[i]*DFDS[i];
                              }
                        DFDEPv=-(M*M*I1*I1o*(1+e)/(LAMDA-
KAPPA));
                        for(i=0;i<6;i++)
                              for(j=0;j<6;j++)
                                    EPM[i][j]=EM[i][j]-
(EMN[i]*EMN[j])/(TRNEMN-DFDEPv*Aii);
                                    for(i=0;i<6;i++){
                                          if(LC[i]==0){
                                                DS[i]=DI[i];
                                                DE[i]=0;
                                          }
                                          else{
                                             DS[i]=0;
                                             DE[i]=DI[i];
                                          }
                                    }
                                    for(i=0;i<6;i++){
                                          if(LC[i]==1){
for(j=0;j<6;j++)
                                                if(LC[j]==0)      DS[j]-
=EPM[j][i]*DE[i];
                                          }
                                    }
                                    for(k=0;k<5;k++){
                                       if(LC[k]==0){
for(i=k+1;i<6;i++){
```

```
                                                    if(LC[i]==0){
y=EPM[i][k]/EPM[k][k];
for(j=k;j<6;j++)
if(LC[j]==0)
EPM[i][j]-=y*EPM[k][j];
DS[i]-=y*DS[k];
                                                    }
                                                }
                                            }
                                        }
                                        for(i=0;i<6;i++)
                                            if(LC[i]==0) n=i;
DE[n]=DS[n]/EPM[n][n];
                                        for(i=n-1;i>=0;i--){
                                            if(LC[i]==0){
                                                y=DS[i];
for(j=i+1;j<=n;j++)
if(LC[j]==0)
y-=EPM[i][j]*DE[j];
DE[i]=y/EPM[i][i];
                                            }
                                        }
                                        for(i=0;i<6;i++){
                                            if(LC[i]==1){
                                                DS[i]=0;
for(j=0;j<6;j++) DS[i]+=EPM[i][j]*DE[j];
                                            }
                                        }

                                        for(i=0;i<6;i++)
if(LC[i]==0)DS[i]=DI[i];
                                            DLAMDA=0;
                                            for(i=0;i<6;i++)
DLAMDA+=(EMN[i]*DE[i])/(TRNEMN-DFDEPv*Aii);
DEPv=DLAMDA*Aii;
//del_I10=?
I1o+=I1o*(1+e)*DEPv/(LAMDA-KAPPA);
e-=(1+e)*(DE[0]+DE[1]+DE[2]);
                                }
                                for(i=0;i<6;i++){
                                    S[i]+=DS[i];
                                    E[i]+=DE[i];
                                }
                                I1=(S[0]+S[1]+S[2]);
                                for(i=0;i<6;i++)
                                    SD[i]=S[i]-(I1*DIJ[i])/3;
                                    J2=(((S[0]-S[1])*(S[0]-S[1])+(S[1]-
S[2])*(S[1]-S[2])+(S[2]-S[0])*(S[2]-
S[0]))/6)+S[3]*S[3]+S[4]*S[4]+S[5]*S[5];
                                    p=I1/3; q=sqrt(3*J2); gama=E[2]-E[0];
                                    std::cout<<std::endl;
                                    for(i=0;i<6;i++)
std::cout<<std::endl<<"S["<<i+1<<"]::"<<S[i];
                                    std::cout<<std::endl;
                                    for(i=0;i<6;i++)
std::cout<<std::endl<<"E["<<i+1<<"]::"<<E[i];
std::cout<<"I1o::"<<I1o<<std::endl; std::cout<<"2*I1::"<<2*I1;
gamaout<<gama*100<<std::endl; pout<<p<<std::endl;
 qout<<q<<std::endl;
 Evout<<-(E[0]+E[1]+E[2])*100<<std::endl;
Eaout<<E[2]*100<<std::endl; count++;
      }
while(count<=2000); gamaout.close(); pout.close();
   qout.close();
   Evout.close();
   Eaout.close();

}
```

SELECT A PROFESSION

CREATIVE	SOPHISTICATED	RECOGNIZED	RESPONSIBLE
ENDURING	UP-TO-DATE	WORLWIDE	IMPORTANT

WWW.GF.UKIM.EDU.MK

OUR FACULTY CAN GIVE YOU

IMPULSE !	SCHOLARSHIPS FOR THE BEST	ASSURANCE !	COORPERATION WITH INDUSTRY AND INTERNATIONAL UNIVERSITIES
SIMPLE ENROLLMENT	MOTIVATION !	100% EMPLOYMENT AND INTERNATIONALLY RECOGNIZED DIPLOMA	SUPPORT !

WWW.GF.UKIM.EDU.MK

ENHANCING SUSTAINABILITY OF RESIDENTIAL BUILDINGS USING QUARRY STONE WASTE AS A BUILDING MATERIAL

Valentina Zileska Panchovska
PhD, Professor
Ss. Cyril and Methodius University in Skopje
Faculty of Civil Engineering
N. Macedonia
valentinazp@gf.ukim.edu.mk
0000-0001-7620-4040

Sead Abazi
PhD, Assistant Professor
Ss. Cyril and Methodius University in Skopje
Faculty of Civil Engineering
N. Macedonia
0000-0001-8263-600X

Todorka Samardzioska
PhD, Professor
Ss. Cyril and Methodius University in Skopje
Faculty of Civil Engineering
N. Macedonia
0000-0001-8992-2279

Igor Peshevski
PhD, Associate Professor
Ss. Cyril and Methodius University in Skopje
Faculty of Civil Engineering
N. Macedonia
0000-0002-2748-5795

Martin Gjorgjieski
MSc, Student
Ss. Cyril and Methodius University in Skopje
Faculty of Civil Engineering
N. Macedonia

Scientific Journal of Civil Engineering (SJCE)

DOI: doi.org/10.55302/SJCE2514139zp

The intensive construction industry drives a demand for use of waste stone as a sustainable construction material. This is result of the goals to decrease the intensity of use of the available natural resources and to increase in utilization of stone waste from quarries. This paper delves with the utilization of waste from the marble mine in the Gjurovo locality near Prilep for construction purposes. Geotechnical testing was carried out on the quarry waste and the possibilities for its use as a construction material were examined. Then, a residential building at a distance of 40 km from the quarry is considered as a case study. Two alternatives were compared for the building: the first one by using conventional construction materials and the second one by utilising stone waste from the quarry. The costs of items where it is possible to use waste stone were compared. The study shows that the costs for earthworks can be reduced by 58%; concrete works by 5%; floors by 25% and facades by 24%. It is calculated that the construction costs for 1 m^2 of the building can be reduced by 6%, compared to the alternative with the conventional materials. The study promises that there are many opportunities for the use of quarry waste as a building material. The use of quarry waste reduces construction costs, which benefits the circular economy and all aspects of sustainable development. The paper also discusses some of the limitations of using quarry waste that should be considered in any project.

Keywords: sustainability, residential buildings, quarry stone waste, cost reduction, circular economy

1. INTRODUCTION

The intensive construction of residential buildings increases the need to use natural stone as a sustainable building material, which leads to a reduction in its available quantities in nature. On the other hand, it also increases the

amount of waste generated during the process of extracting and shaping stone, as well as the energy embodied in the products obtained by its use.

Regardless of the method used for natural stone extraction, during the cutting and shaping of the blocks into a final product, approximately 20-30 % of the volume/weight of each unit is lost [1]. The waste generated is not only solid waste, but there is also slurry waste which is mainly obtained from the technological process of obtaining the required final product. In practice, If not used for other purposes, space for planned disposal is provided for this waste. The amount of such waste is constantly increasing and has a negative impact on the environment, human health and other aspects of sustainable development [2]. Instead of its disposal, it is of global interest to find sustainable solutions for its application.

The use of quarry waste, both solid and slurry, for application in new products is not a novelty. This material can be used in construction and other industries as a resource for obtaining various products [3, 4]. The solid stone waste can be used as floor/wall tiles with irregular or regular shape or as a buffer, the marble flour (white powdered limestone) can be used in tile glue, the marble powder can be used to prepare glass-polyester composites etc. [5]. This will not reduce only the permanent destruction of natural stone deposits, but it will also reduce the CO_2 emissions from the stone extraction and shaping processes [6]. From that point of view, when the material is from a local quarry, it has an additional advantage in the reduction of transport distances and costs. Furthermore, this approach stimulates the local economy in sustainable manner. The end result is an improvement of the products sustainability and if it is a construction material, it also contributes to the sustainability of the buildings. However, despite numerous conducted researches to use the marble quarry waste as a construction material or for production of new products, there are few studies focused on the economic aspect of its use, especially on the impact on building construction cost. Therefore, the aim of this paper is to investigate the possibilities of using marble quarry waste as a local construction material and assess its impact on the sustainability and total costs of the building construction.

2. LITERATURE REVIEW

A review of published research and reports regarding structural applications of marble and granite powder quarry waste is given in [5]. It was observed that using that waste positively affects the physical and mechanical properties of the concrete. At the same time, construction costs are reduced by a certain amount. These findings are confirmed by other studies. They have proven that in the construction industry, solid coarse and fine waste, not only from quarries but also from the demolition and deconstruction of buildings (concrete, metal, bricks, etc.), can be used for the preparation of concrete, as coarse and fine aggregate, for partial replacement of cement and for other purposes [1, 7-10].

Kore et al. present a review on sustainable utilization of marble waste for concrete preparation [7]. They concluded that there was no negative impact on the properties of concrete or mortar by replacing cement with marble powder by 10%. Furthermore, that combination of marble waste and fly ash as a binder was found to be more beneficial than just using marble waste for replacement of Ordinary Portland Cement (OPC). According to the authors, marble waste can be used to replace fine and coarse aggregate in the range of 50% and 75%.

The research of *Qamer et al*. [8] presents the results of the mechanical and long-term properties of concrete using dimensional stone from marble waste as a component for concrete. The results, compared with the properties of conventional concrete, showed that coarse and fine aggregates can be replaced with marble waste in large quantities. A mixture of marble powder waste and fly ash was proposed for binder, rather than simply replacing it with Portland cement. Furthermore, the study [11] focuses on the dried waste marble powder used for partial replacement of cement in concrete. The authors developed mathematical models based on statistical methods and experimental results. They proposed guidelines for the use of marble powder as a partial replacement of cement in concrete.

Another research by *Mangi et al. was* focused on usage of waste of marble and ceramic tiles for partial replacement of aggregate and binder [9]. It was found that concrete made using such waste is durable and strong. *Patil et al.* used waste marble sand to replace the 1-2 mm size aggregates in concrete [12]. The strength of their concrete was higher compared to conventional concrete.

The study [13] focuses on mortar production using waste marble powder as a partial

replacement for cement. The authors concluded that mortar with the proper use of waste marble powder as a filler is a low-cost material and is beneficial for both the environment and the stone industry. In this regard, it was noted in [14] that the dimensional stability and durability of mortar could be improved by replacing the mortar paste with waste marble powder.

The usage of fine waste marble powder in pozzolanic concrete to increase the sustainability of the concrete is presented in [15]. The cost-efficiency analysis showed that embodied CO_2 emissions can be reduced by using silica fume binder and waste marble powder in concrete. In addition, the physical properties of the concrete are improved, and the reduction in the disposal of marble waste provides economic qualifications and environmental benefits. A similar study was presented in [16], where marble powder was used for partial replacement of cement in concrete. According to the results of the compressive strength test, it was identified that a decrease in compressive strength was observed with an increase in the content of marble powder in the test specimens.

Regarding cement, the study [17] focused on the density, porosity and mechanical properties of a new class of inorganic polymer cements made with local marble waste powders. The results of the research showed that the cements have a low carbon footprint and can be used as low-density, low-temperature binders for sustainable construction. Granite quarry powder was used in the research presented in [18]. The results of the research showed that replacing cement with 10% or 20% granite quarry powder was not detrimental to the durability of the product.

The use of marble powder for the production of bricks for exterior and interior walls is presented in [3]. It has been found that waste marble powder can replace 5–30% of the clay, resulting in polished elements that have good construction performance and are more sustainable than conventional ones. Another solution for the use of marble and granite waste (fragments and powder) is to produce artificial marble. By using crushed fragments as a load, powder as a filler and adding polyester resin, the materials can be mixed and then compacted [19]. This product is economical and has mechanical and physical properties that are satisfactory for its use as a building material in structural and bearing members.

Therefore, it can be concluded that there are numerous studies on the use of mine waste from marble and granite, but they are focused mainly on the physical characteristics of the products where they are used. There are a small number of studies that focus on the combination of sustainability and economy aspects of the use of quarry waste as a building material in structures, which is explored in this paper.

3. MATERIALS AND METHODS

A residential building is selected as a case study to investigate the opportunities of using a quarry waste from local quarry as a construction material. The building is located in the city of Prilep, Macedonia, 40 km away from the quarry in question. The first analysed alternative for the building is construction with conventional materials, for which a bill of quantities and cost estimation are available [20]. As a second alternative analysed, a bill of quantities and costs is prepared for the items where it is possible to replace the conventional material with construction material prepared from quarry waste of the required quality. The comparison of the two alternatives is focused on the construction costs and associated sustainability.

3.1 PROPERTIES OF THE WASTE FROM QUARRY GJUROVO

For the quarry Gjurovo, Figure 1, near the city of Prilep, waste rock samples were tested.

Figure 1. Waste stone from quarry Gjurovo, near the city of Prilep

The aim of the tests was to determine the physical, mechanical and mineralogical-petrographic characteristics of the stone and to assess the suitability of the material for its application in construction as a building material. There is waste material in the quarry

that cannot be processed in production. In addition, about 40 m^3 of dry sludge is produced per month. The marble sludge or powder in the production itself (cutting the finished product from marble tiles using water) is collected in the marble sludge purifier.

3.1.1 Physical and mechanical properties of the waste stone

By examining the physical and mechanical properties of the waste stone, results were obtained for the following parameters [21]:

- Compressive strength in a dry state;
- Compressive strength of water-saturated samples;
- Water absorption;
- Bulk density with pores and cavities;
- Bulk density without pores and cavities;
- Bulk density coefficient;
- Porosity, frost resistance.
- Obtained results and respective test MKS standards are presented in Table 1.

Table 1. Results for physical and mechanical properties

No	Property	Test standard according to MKS	Symbol	Symbol	Values	Quality Requirements: CON/MKS B.B2.009 BNS/MKS U.E9.021/028 RC/MKS U.E9.028
1.	Compressive strength in a dry state	B.B8.012	MPa	σ_{pmin}	129,50	CON/min. (80; 160) BNS/min. (140) RC/min. (120, 140; 160) Pad/min (100; 120)
				σ_{pmax}	160,80	
				σ_{pmed}	142,80	
2.	Compressive strength of water-saturated samples	B.B8.012	MPa	σ_{pmin}	121,40	CON/min.(64; 128) BNS/n.(100)
				σ_{pmax}	154,10	
				σ_{pmed}	135,80	
3.	Compressive strength after 25 freeze-thaw cycles	B.B8.012	MPa	σ_{pmin}	115,80	Max. 25 % lower compressive strength than standards
				σ_{pmax}	152,60	
				σ_{pmed}	128,00	
4.	Water absorption	B.B8.010	%	U	0,18	CON/max.(1.0) RC/max.(0.75; 1.0) Pad/max. (1,0)
5.	Abrasion resistance	B.B8.015	cm^3/ 50 cm^2	A_b	19,0	CON/max.(35.0) RC/max. (12.0, 18.0; 35.0)
6.	Bulk density with pores and cavities	B.B8.032	kg/m^3	γ_r	2720	(2000 - 3000) kg/m^3
7.	Bulk density without pores and cavities	B.B8.032	kg/m^3	γ_z	2760	(2000 - 3000) kg/m^3
8.	Density	B.B8.032	%	G	98,6	/
9.	Porosity	B.B8.032	%	P	1,4	/
10.	Persistence of frost action	B.B8.001	Damages and losses / % /	M	No damage and little mass loss of 0,2 %	CON/max. (5.0) RC/max. (5.0) Pad/ max. (10.0; 12.0)

3.1.2 Mineralogical-petrographic analysis

The mineralogical-petrographic analysis was carried out on the samples, which were macroscopically and microscopically examined and described. The microscopic examination was carried out with a polarized optical microscope with transmitted light.

Macroscopic description: The sample is a light grey rock that is compact, solid, and has a microcrystalline structure and a massive texture. When treated with cold dilute of hydrochloric acid (HCl), it reacts violently, indicating a calcite composition. The sample shows thin calcite veins and cracks, rarely filled with limonite.

Microscopic description: The microscopic examination of the petrographic preparation determined that the rock is characterized by a microcrystalline structure and has a granular texture. The rock is characterized by a mono-mineral composition, i.e. almost completely composed of calcite. Very small amounts of quartz and very rare limonite have been found. The calcite crystals are very small and generally occur in allotriomorphic form with sizes up to about 100 pm (Figure 2). Calcite veins with a thickness varying from 2-5 mm are often present. Larger crystalline calcite are within the veins, which reach a size of about 2 mm. A very small presence of quartz has been determined, which appears without any particular regularity in the form of irregular, rounded crystals with a size of 50-100 pm. The very rare presence of micro cracks has also been noted, which are filled with a small amount of tiny brownish-reddish limonite grains.

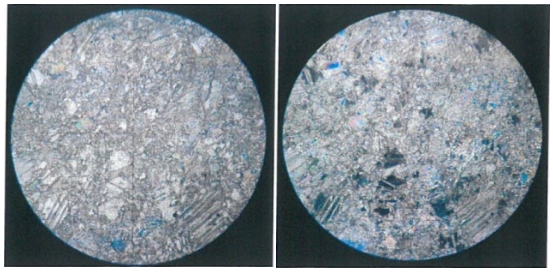

Figure 2. Micro-crystalline calcite, II nicoli (left), X nicoli (right)

3.1.3 Possibilities for application of quarry stone waste

According to the legal regulations in Macedonia, there are no restrictions on the application of waste from quarries as a construction material, as long as it meets the requirements determined by the relevant MKS standards. Furthermore, according to the determined physical and mechanical properties, as well as the mineralogical-petrographic analysis of the examined stone from the quarry, the material is suitable for use for construction purposes, i.e. as building material. The properties of the stone are in accordance with the stone quality requirements given in the relevant Macedonian standards (MKS standards). In addition to obtaining plates and elements/products with different dimensions and shapes, the remaining waste rock can be used as aggregate for concrete, asphalt, mortar, concrete blocks, buffer, for floors, partial replacement of cement, as a raw material for production of glue for tiles and for other construction purposes, after adequate research. In concrete, according to the tests, marble stone waste could be used in two cases: as a replacement for the aggregate and as a partial replacement for the cement.

3.2 DESIGN OF THE BUILDING WITH CONVENTIONAL MATERIALS

The designed building is for collective housing - apartments building, Figure 3, with reinforced concrete (RC) structural system with the following characteristics:

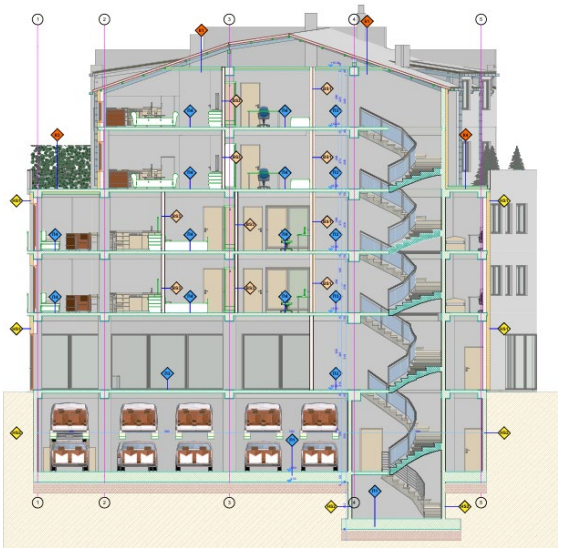

Figure 3. Cross-section of the building

- Number of floors is 6;
- Area of the construction plot is A=548 m^2;
- Gross area under the building is A=327.14 m^2;
- Total net area A=1470.51 m^2;
- The walls in the levels below the terrain elevation are designed as RC walls and RC stair core;
- The external walls are made of lightweight blocks with d=16cm, with a thermal insulation of expanded polystyrene;
- The floors are finished depending on the purpose: granite tiles for the business premises, stairs, entrance hall and hallway, floors in the garages are made of concrete, ceramic tiles are provided for the bathrooms and terraces, while laminate flooring is

provided in the apartments. For the ground floor – interlock pavers (behaton) are designed;

- The roofing is designed with sandwich roof panels with a slope of 15% and 35% placed on a steel roof structure. Solar roof panels are designed in one part of the roof;
- The exterior doors and windows are provided with PVC profiles, except on the ground floor where a glass facade with aluminium profiles is provided.

4. RESULTS AND DISCUSSION

A bill of quantities and costs was available for the building alternative with conventional materials, presented in [20]. Then, for the same building, an alternative design was prepared, where, for the items where it was possible, conventional materials were replaced with materials prepared by using stone waste from quarry. The calculations were made for use of the waste stone in earthworks, concrete works, floors, walls, and facade works. Respecting the law, the price of this local material was determined by the concessionaire of the quarry.

By comparing the costs for the two alternatives, the following reductions of the costs are calculated (Table 2):

- For earthworks - backfilling under the foundation slab and pavements, costs were reduced by 58%.
- For the preparation of concrete, the replacement was made for the following aggregates: 205 kg/m^3 for the 2nd fraction of 4-8 mm, 372 kg/m^3 for the 3rd fraction of 8-16 mm and 588 kg/m^3 for the 4th fraction of 16-32 mm, or 1135 kg aggregate in total for one cubic meter of concrete. After transporting the aggregate from the quarry, the concrete mixture can be done by mixer. The installation of the concrete can be perform with pump, with wooden formwork positions. The concrete works for the building were reduced by 5%.
- In floors and walls, a cost reduction was made by replacing ceramic tiles with marble tiles, partially using marble powder for glue. The costs were reduced by 25%.
- In facade works – the quarry stone waste was used as a partial replacement of the aggregate and for the glue. The costs were reduced by 24%.

The comparison of the variants proves that by using quarry waste as a construction material, the total costs of building construction are reduced by 6% (Table 2).

Table 2. Costs reduction when using waste marble stone

	Earthworks	Concrete	Floors and walls	Facade	Per 1 m^2 built-up area of the building
Costs reduction	58.00 %	5.00 %	25.00 %	24.00%	6 %

The results presented in Table 2show that the use of local waste stone material, which is of the required quality, reduces the costs of building construction. However, the results obtained confirm the results of other researchers who emphasize that the use of quarry waste in a certain amount fulfils the needed properties as a building material, reduces material costs, stimulates the local economy, social development, and is favourable for the environment and sustainable development in general [5, 22, 23].

5. CONCLUSIONS

Urbanization is characterized by the intensive construction of residential buildings. It contributes to improving people's living standards, but causes an increased demand for resources and raw materials for construction. Therefore, limited natural resources are being depleted and environmental pollution is increasing. On the other hand, quarry stone waste is a global problem due to the large quantities produced daily and due to its degradation and possible negative overall effects on the environment and human health. Therefore, the need to use it for other purposes is in the interest of sustainable development. Furthermore, the concrete produced by using marble waste is eco-friendly and economical construction material due to the low cost of the marble stone waste.

Using stone waste with required quality from a local quarry is a sustainable practice. This contributes to ensuring good use of natural resources and minimal environmental impact, which is in favour to the sustainability of the buildings.

An additional benefit is that the use of local materials reduces their carbon footprint trough reducing transportation distances, allowing the necessary building materials to be available "just in time". The increased use of local waste quarry materials would positively impact the number of jobs, primarily at the local level. It stimulates the local economy, contributes to environmental protection and raises awareness among employees about the importance of sustainable development and many other positive aspects of economic, social and environmental sustainability. The results of this research can be used as experience for further research.

The limitation of the research is that it isfocused on one case study - the use of waste from the Gjurovo quarry for construction of residential building. For further research, it is proposed to increase the number of analysed buildings, combine quarry waste products with other materials, compare the results with analyses for other types of buildings and structures (geotechnical, hydrotechnical), etc.

REFERENCES

[1] Vashi, J., Daftardar, A. (2024),"Sustainable concrete with optimum use of waste marble powder", in Proceedings of International Conference on Advancements in Construction Materials (ICACM2023), India, July. 2024, Vol. 3146, No. 1, 020004.

[2] Polydorou, T., Kyriakides, N., Neocleous, K., Hadjimitsis, D. (2022), "Handbook of Sustainable Concrete and Industrial Waste Management, 14 - Use of quarry waste in concrete and cementitious mortars", Woodhead Publishing, pp. 289-304.

[3] Suffian, M., Ullah, S., Ostrowski, K. A., Ahmad, A., Zia, A., Wieczorek, K., Awan, A. A. (2021), "An experimental and empirical study on the use of waste marble powder in construction material," Materials, Vol. 14, No. 14, 3829.

[4] Tazzini, A., Gambino, F., Dino, G. A., Casale, M. (2024), "Managing Marble Quarry Waste: Opportunities and Challenges for Circular Economy Implementation", Sustainability, Vol. 16, No. 7, 3056.

[5] Nayak, S. K., Satapathy, A., Mantry, S. (2022), "Use of waste marble and granite dust in structural applications: A review," Journal of Building Engineering, Vol. 46, 103742.

[6] Zhang, X., Yin, J., Li, F. (2023), “Research on the reduction of carbon emissions in buildings by specifying low-carbon concrete mixes in China,” Proceedings on Engineering Sciences, Vol. 17, No. 4, pp. 655-666.

[7] Kore, S. D., Vyas, A. K.,Kabeer K. I., S. A. (2020), "A brief review on sustainable utilisation of marble waste in concrete," International Journal of Sustainable Engineering, Vol. 13, No. 4, pp. 264-279.

[8] Qamer, M., Rafique, M. A., Billah, M. B., Usman, M., Haider, W., Ashraf, A., Shad, M. A., Ibrahim, M. (2022), "A comprehensive review on the use of marble waste in concrete," International Journal of Advance Industrial Engineering, Vol.10, No.3, pp. 37-44.

[9] Mangi, S. A., Raza, M. S., Khahro, S. H., Qureshi, A. S., Kumar, R. (2022), "Recycling of ceramic tiles waste and marble waste in sustainable production of concrete: a review, " Environmental Science and Pollution Research, Vol. 29, pp. 18311–18332.

[10] Berdoudi, S., ElharrachH. B., Hebhoub, H. (2017), "Valorization and recycling of quarries waste as an addition in cement," IstrazivanjaiprojektovanjazaPrivredu, Vol. 15, No. 2, pp. 122-127.

[11] Singh, M., Srivastava, A., Bhunia, D. (2019), "Analytical and experimental investigations on using waste marble powder in concrete," Journal of Materials in Civil Engineering, Vol. 31, No. 4, 04019011.

[12] Patil, A., Pillai, A. A., Nair, A. P. (2022), "Use of waste marble sand in concrete, "International Research Journal of Engineering and Technology (IRJET), Vol. 9, No. 7, pp. 2614-2618.

[13] Benjeddou, O., Alyousef, R., Mohammadhosseini, H., Soussi, C., Khadimallah, M. A. Alabduljabbar, H., Tahir, M. M. (2020), "Utilisation of waste marble powder as low-cost cementing materials in the production of mortar", Journal of Building Engineering, Vol. 32, 101642.

[14] Li, L. G., Huang, Z. H., Tan, Y. P., Kwan, A. K. H., Liu, F. (2018), "Use of marble dust as paste replacement for recycling waste and improving durability and dimensional stability of mortar," Construction and Building Materials, Vol. 166, pp. 423-432.

[15] Ince, C., Hamza, A., Derogar, S., Ball, R. J. (2020), "Utilisation of waste marble dust for improved durability and cost efficiency of pozzolanic concrete," Journal of Cleaner Production, Vol. 270, 122213.

[16] Khan, K., Ahmad, W., Amin, M. N., Ahmad, A., Nazar, S., Alabdullah, A. A., Arab, A. M. A.(2022), "Exploring the use of waste marble powder in concrete and predicting its strength with different advanced algorithms", Materials,. Vol. 15, No.12, 4108.

[17] Kamseu, E., Akono, A. T., Rosa, R., Mariani, A., Leonelli, C. (2022), "Valorization of marble

powder wastes using rice husk ash to yield enhanced-performance inorganic polymer cements: Phase evolution, microstructure, and micromechanics analyses," Cleaner Engineering and Technology, Vol. 8, 100461.

[18] Medina, G., Sáezdel Bosque, I. F., Frías, M., Sánchez de Rojas, M. I., Medina, C. (2018), "Durability of new recycled granite quarry dust-bearing cements," Construction and Building Materials, Vol. 187, pp. 414-425.

[19] Attia, H. A., Farghaly, M. G., Saleh, A. M., Khalek, M. A. A. (2024), "For sustainability and a green environment: artificial marble granite as a value-added product from marble and granite waste residue", Journal of Al-Azhar University Engineering Sector, Vol. 19, pp. 254 - 268.

[20] Basic design of a residential building, Designers: Geniko - Prilep, Investor Mermer Imperial – Prilep, tech. No. 129/2022.

[21] Test report: Physical - mechanical properties and mineralogical - petrographic analyses of rock stone, AGI 09/21-1724, 2021 (in Macedonian).

[22] Singh, M., Choudhary, K., Srivastava, A., Sangwan, K. S., Bhunia, D. (2017), "A study on environmental and economic impacts of using waste marble powder in concrete," Journal of Building Engineering, Vol. 13, pp. 87-95.

[23] Parekh, R., Norford, L., Hughes, J. (2024), "Sustainable multi-story building design utilizing recycled marble and ceramic waste," World Journal of Advanced Research and Reviews, Vol. 23, No. 3, pp. 2879–2883.

Mitko Srbakoski
MSc in Civil Engineering
Hellas Construction
Texas, USA
mitkosw@gmail.com

Jovan Br. Papić
PhD, Professor
Ss. Cyril and Methodius University in Skopje
Faculty of Civil Engineering
N. Macedonia
0000-0002-2952-302X

POTENTIALS FOR OPTIMIZATION OF RETAINING WALLS' DESIGN

The idea for the paper arises from the evolution of the interpretation of the soil's shearing resistance, which later reflects in the calculation of earth pressures and the design of retaining walls. There, according to the National Annex to Eurocode 7 (EC7), only the active, not the passive earth pressure, is considered. Namely, although traditionally the failure envelope of the Mohr's stress circles for soils is adopted as linear and inclined, in the scientific community, it has increasingly been treated as a non-linear function. Therefore, within the paper, their analysis and comparison is carried: a theoretical review is given for the linear and non-linear failure envelopes, after which a methodology for determination and application of non-linear shearing resistance in software is described, offering possibility for comparison of results for the amounts of active earth pressure forces (E_a) obtained by applying parameters from the interpretation of laboratory tests of fine-grained soil material with linear and non-linear failure envelopes in the design of retaining walls with certain heights.

Keywords: shearing resistance, non-linear failure envelope, earth pressure, Eurocode 7

1. INTRODUCTION

The purpose of this paper is to offer an advanced, but insufficiently applied approach for the calculation of active earth pressure on retaining walls. Namely, when interpreting the shearing resistance of soils, the theory of Mohr-Coulomb-Terzaghi is most often used, with which it is assumed that the linear function is a sufficiently accurate description of soil's failure in total domain of stresses: both below and above those applied during laboratory investigations. However, numerous tests in a wide stress domain have undoubtedly shown that the failure envelope is not linear. Thus, the behavior of the soil under a different range of normal stresses indicates doubt in the constancy of the angle of internal friction for any state of stresses for the same soil material, which is why, between the many geotechnical structures and works, the analysis of actions on retaining walls will have to undergo changes.

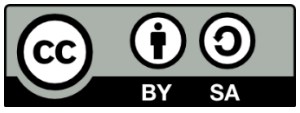

Namely, as there is difference in the shearing resistance parameters determined through linear and non-linear failure envelopes, the same applies to the earth pressures on the retaining walls, especially in the zone of low stresses, since such are most common behind them. In the paper, a comparison of these two theories for interpretation of shearing resistance and their influence on the active earth pressure is made.

2. REVIEW OF SOIL'S SHEARING RESISTANCE THEORIES

2.1 LINEAR MOHR-COULOMB-TERZAGHI FAILURE ENVELOPE

One of the most commonly used relations for interpreting shearing resistance τ of soil materials, defined by ϕ' – angle of shearing resistance, and c' – cohesion, in routine geotechnical practice is the Mohr-Coulomb's law, later modified by Terzaghi who separated the total normal stresses σ and pore pressures u, which is fundamental in geotechnics:

$$\tau = c' + (\sigma - u) \cdot \tan\varphi' \qquad (1)$$

However, this theory simplifies the shearing strength of soils because it assumes constant and unaffected parameters over the entire range of loads.

2.2 NONLINEAR FAILURE ENVELOPE OF HYPERBOLIC TYPE

The non-linear failure envelope [5] provides answers to some of the limitations of the linear one [6], particularly its inability to represent the behavior of soils under different stress states, especially those not applied during the test. It introduces a non-linear relationship between the normal stress and the shearing resistance, and at the same time expresses the strength only through angle of shearing resistance which changes magnitude as a function of the normal stress (i.e., variable angle and no cohesion). The general form of the non-linear failure envelope of the hyperbolic type can be expressed as:

$$\tau = \sigma'_n \cdot \tan\phi'_{\sigma'_n} \qquad (2)$$

From the stress perspective, the fracture mechanism is further complicated by the constant contact between the grains in the material, which causes the grains to move and slide under the action of normal stresses, and the fact that the local stresses in the material between the grains, which can be several times greater than the total stress of the entire material, also causes the grains to crush and break. This phenomenon is the cause of differences in the peak strength of the soil and the strength at large deformations. Taking all this into account, the previous relationship is more precisely expressed by

$$\tau = \sigma'_n \cdot \tan\left(\varphi_B + \frac{\Delta\varphi}{1+\frac{\sigma_n}{p_N}}\right) \qquad (3)$$

where:

ϕ'_B - basic friction angle, which represents the angle of shearing resistance that occurs at high stresses, when there is no change in the volume of the material, but the developed stresses lead to their breakage. When the stresses are complete and do not change magnitude, then this angle reflects the friction at constant volume ϕ'_{cv}.

$\Delta\phi'$ - is the maximum angular difference, which in soils with compactly arranged grains considers the effect of dilatancy ($\phi'_B+\Delta\phi'=\phi_0$ – initlal, maximum, angle), and reflects compactness and roundness, while in those with high percentage of flat grains, at large deformations, it expresses an imperfect arrangement of the grains relative to the shear plane, at almost "zero" normal stresses.

p_N - stress that expresses the strength of grains against crushing, which depends on the compactness, grain size distribution, mineralogical composition and grains' shape.

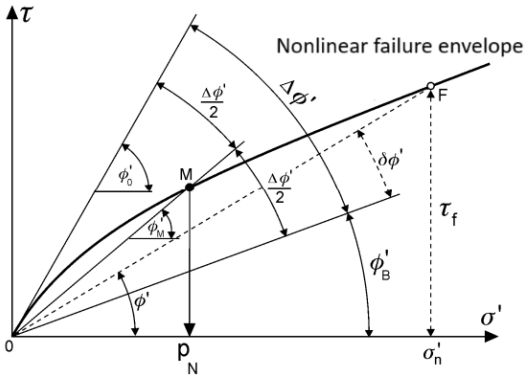

Figure 1. Parameters of a non-linear failure envelope of hyperbolic type

3. WORK METHODOLOGY AND ANALYZED CONDITIONS

The difference in the application of linear and non-linear failure envelopes will be examined through a design of reinforced concrete cantilever retaining walls, under previously defined conditions:

- Geomechanical conditions – in order to threat non-linearity for laboratory-defined material characteristics.
- Geometric conditions – different heights of the structure. The non-linearity of the failure envelope is mostly pronounced in the zone of relatively small normal stresses, like those that occur up to certain depths behind retaining walls.

The values of Ea are calculated for shearing resistance parameters determined with both strength theories. In the case of a linear failure envelope, the shearing resistance parameters (φ', c') are constant along the height of the retaining wall, so in conditions of fine-grained materials, both parameters are taken to determine the amount of active earth pressure. On the other hand, the interpretation with a non-linear failure envelope is made in the NENVE software using a hyperbolic type of curve: a variable shearing resistance angle is determined, which decreases from ϕ_0 to ϕ'_B as the normal stresses rise, while the "cohesion" does not exist. In it, the normal stresses applied in laboratory experiments are entered, as well as auxiliary angles determined geometrically from the test results [7-8]. In the output section, in addition to the parameters of the non-linear failure envelope (basic angle, angular difference, stress), the software offers a range of diagrams, and of interest to the research in question are those where the relationship between the shearing resistance angle and the normal stresses is given. As mentioned, the angle ranges from initial (maximum) value ϕ_0 to basic angle (minimum) ϕ'_B, noting also the importance of p_N. The dependence can be displayed both on a linear and semi-logarithmic scale, from which the shearing resistance angles for different stress levels can be simply readout, which is what was done. Namely, in the calculations for Ea, the shearing resistance angle varies depending on the normal stress that grows with depth. Therefore, in the calculation of Ea, in the theory of the non-linear failure envelope, the soil material is divided into fictitious layers with a thickness of 1 m. Once the normal stresses in the middle of these layers have been determined for the laboratory-derived bulk density, these values are applied to the output diagrams from NENVE in order to readout for the angles: this procedure takes into account the change in angle, which value is later assigned to the corresponding layers, and for such an amount of shearing resistance angle – the Ea is determined.

3.1 GEOMECHANICAL CONDITIONS

Within the framework of the paper, findings from analyses performed with parameters interpreted from direct shear tests on fine-grained material (in practice called "coherent") are presented. In order to "fulfill" the conditions for effective stresses and drained conditions, it is assumed that there is a drainage system with perforated pipes on the back of the wall and that the groundwater level is deep. Below are excerpts from conducted tests for the analyzed fine-grained material.

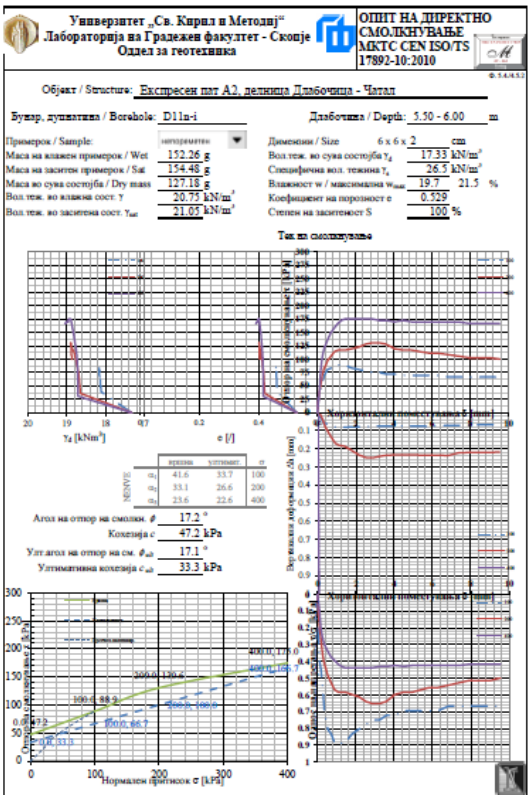

Figure 2. Parameters obtained from direct shear test conducted on fine-grained material

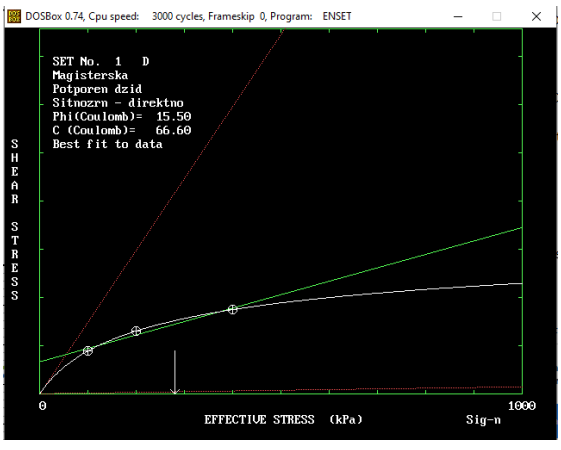

Figure 3. Interpretation with linear failure envelope in the NENVE software

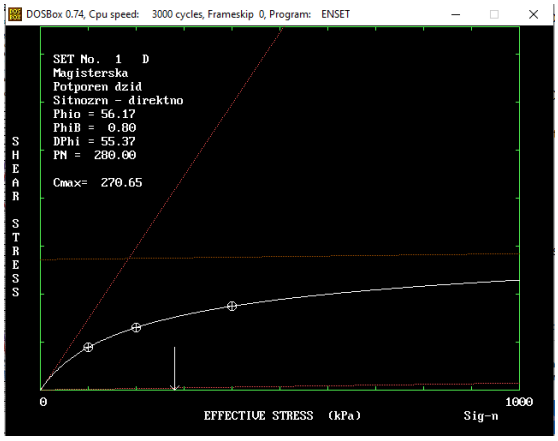

Figure 4. Parameters of non-linear failure envelope of hyperbolic type in the NENVE software

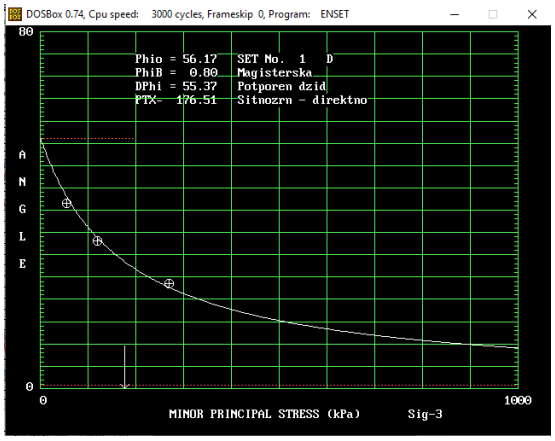

Figure 5. Relationship between angle of shearing resistance and normal stresses (NENVE)

Linear failure envelope (constant parameters)		Non-linear failure envelope of hyperbolic type (variable parameters)	
Angle of internal friction ϕ' [deg]	Cohesion c [kPa]	Initial angle of shearing resistance ϕ_0 [deg]	Mean stress p_N [kPa]
17,2	47,2	56,17	270,65

Table 1. Shearing resistance parameters of tested fine grained material interpreted with linear and non-linear failure envelopes

3.2 GEOMETRICAL CONDITIONS

Retaining walls with heights h=2-10 m, foundation widths B=0.6h and constant thickness of structural parts of 0.1h for the wall face and 0.15h for the footing, are modeled in the GEO5 software, with the soil parameters conditions given above, both for constant and variable strength parameters, including unit weight of 20,75 kN/m^3, through equilibrium boundary conditions.

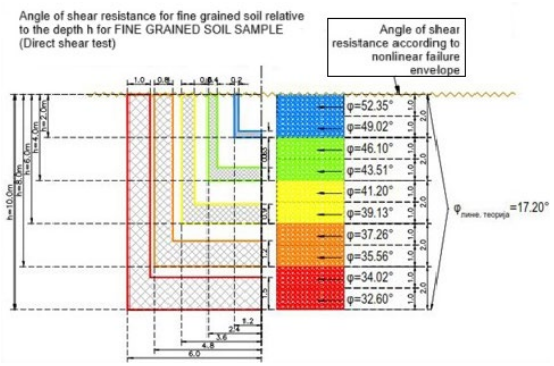

Figure 6. Geotechnical model: overview of geometrical conditions of the retaining wall and geomechanical conditions with constant and variable shearing resistance parameters

4. FINDINGS FROM NUMERICAL ANALYSES

According to the parameters determined through linear (constant shearing resistance parameters) and through non-linear failure envelope (angle of shearing resistance as a function of normal stresses), Ea are calculated. In addition, for the non-linear failure envelope, due to the height of the wall, the angle would continuously decrease to some value at a constant volume. The variable angle is applied to fictitious "layers" with a thickness of 1 m, according to the findings of NENVE (for calculated normal stresses in the middle of "layers", angles are read from Figure 5). The corresponding angles thus calculated, depending on the depth of the "layer", are shown in Figure 6. Similarly, the value marked on the drawings as "φ-lin. theory" represents the angle of internal friction obtained from laboratory experiments, which fixed value obtained from a linear failure envelope is used together with cohesion in parallel calculations for Ea, both of them in GEO5.

So, the presented parameters are applied in the GEO 5 software module for the described cantilever retaining walls, where the active earth pressure forces are calculated according to former Macedonian standards (MKS), Design Approach 2 (DA2) of EC7 and Design Case 1 (DC1) with Resistance Factor Approach (RFA) of EC7 2025, which is the same as DA2 of EC7 [1]. The comparison of the force values for all walls, both theories and design procedures, is given in Table 2.

The failure envelopes and their influence on Ea are also reflected in the safety factors for various stability analyses, interpreted through the MKS, EC7 and EC7 2025 [8], which part, however, will be omitted here.

Para-meters inter-preted with	Active earth pressure force [kN] at wall with height [m]				
failure envelope	2m	4m	6m	8m	10m
Linear	/	5,19	39,89	123,83	259,17
Non-linear	/	/	4,56	22,90	71,32

Table 2. Forces of active earth pressure acting on retaining walls with different heights – comparison between values obtained with parameters determined through linear and non-linear failure envelope

From the comparison of the values of active earth pressure forces calculated according to DA2 of EC7, which is reflection of the so-far applied MKS, and the DC1 with RFA of EC7 2025, which is in detail given in [8], it is observed that:

- Calculations according to MKS, DA2 and DC1 give mutually literary the same results when applying linear and non-linear failure envelope;

- Values of Ea obtained with a variable angle of shearing resistance are smaller than those calculated with constant parameters (due to the presence of pronounced cohesion, a larger difference in Ea occurs).

- The increase in E_a is smaller in the case with variable parameters due to the dilatancy, and thus a larger angle of shearing resistance in a long stress range.

- from Ea values it can be seen that in this particular case, at a variable angle of shearing resistance, for heights up to 4 m, there is no need for a support/wall.

- It should also be noted that Ea does not act at vertical plane, but the software treats action at an inclined one, even though the width of the foundation is greater than H·tan(45+φ/2).

5. IMPLICATION

Among the other, the presented findings also affect the material consumption. Thus, as far as reinforcement at the retaining wall is concerned, by applying shearing resistance parameters determined through non-linear failure envelope, in addition to the fulfilled stability conditions, a significant saving in reinforcement can be achieved, which indicates that solid optimization in terms of the thicknesses of the structural elements is also possible!

For example, in the specific case, for a wall height of 10 m, when modeling the soil with shearing resistance parameters obtained through linear failure envelope, the calculations in GEO5 require about 3000 mm^2 of reinforcement, while by applying variable angle, there is almost no need for reinforcement due to the sufficient strength of the soil and assumed dimensions of the wall.

Another view of the results will be given from the aspect of the action of Ea. Namely, all previous results, analyses and comments refer to an inclined plane, which treats the plane on which Ea acts as an inclined surface at angle α=(45-φ/2), although the width of the foundation (0.6H) is greater than H·tan(45+φ/2). However, the GEO5 software package offers the possibility to manually adopt the force to act on a vertical (virtual) plane, which was done within the framework of the research, when all calculations were repeated for the action of a force on a vertical plane. Below is table for comparing the values of the active earth pressure forces calculated by applying DA2 of EC7, i.e. DC1 of EC7 2025, for parameters determined through both theories, as well as for both planes, for mid and maximum heights of the wall.

Height H [m]	6				10			
Plane	I		V		I		V	
Failure envelope	L	NL	L	NL	L	NL	L	NL
Value of Ea [kN]	39,89	4,56	/	/	259,17	71,32	/	/

Table 3. Comparison of forces of active earth pressure Ea for retaining walls with heights 6 m and 10 m achieved for inclined and vertical planes of action when applying parameters determined from linear and non-linear failure envelopes for fine grained material (Legend: 'I' stands for Inclined, 'V' stands for Vertical, 'L' stands for Linear and 'NL' stands for Non-linear).

From table 3 it can be seen that Ea on an inclined plane are many times higher than those on a vertical plane, according to the two theories, where the differences and amounts vary with increasing wall height.

Similar comparison is made also for safety coefficients [8], but it is out of the scope of the paper.

6. CONCLUSIONS

When designing geotechnical structures, typical engineering practice is to apply soil's shearing resistance parameters determined

through linear interpretation of failure envelope, e.g. constant angle of internal friction and cohesion. Such can be valid for the span of loads applied during the laboratory test used for determination of shearing resistance. However, in the case of loads below and above those, and not rarely even within them, such approximation might not be satisfying. In such circumstances and for such purposes, interpretation with non-linear failure envelope is necessary and recommended. One of them is the one of hyperbolic type: it results with angle of shearing resistance which varies (decreases) as the stress increases, while there is no cohesion. This is especially important for the zones of loads below those applied during the test, which appear behind retaining walls and until certain depth at slopes and are as such important in these cases, due to mis-interpretation of shearing resistance.

The difference in the shearing resistance parameters determined through linear and non-linear failure envelopes reflects to the earth pressures on the retaining walls. The paper gave comparison of values of forces obtained at retaining walls with heights 2-10 m by applying parameters determined by these two theories for a fine grained material.

The methodology for modelling variable angle of shearing resistance along the height of the wall is described in detail.

The parameters determined by linear and non-linear failure envelope are included in the GEO 5 software for the mentioned cantilever walls, where the Ea is calculated according to MKS, DA2 of EC7 and DC1 with RFA of EC7 2025. By comparing their values, it was found that DA2 and the DC 1 result in same values of Ea, both when applying linear and non-linear failure envelope parameters. Also, the values of Ea obtained with a variable angle of shearing resistance are smaller than those calculated with constant parameters, while the increase in E_a is smaller in the case with variable parameters.

All these findings support the future application of the new generation of Eurocode 7 and stimulate the use of advanced shearing resistance theories in engineering practice in order to optimize the design of retaining walls.

REFERENCES

[1] Andonov Sarev A.; (2022); Tendencies in the development of Eurocode 7 and in the design of geotechnical structures; Master thesis; Faculty of civil engineering; Skopje (in Macedonian)

[2] Bond A.; (2015); Planned changes in Eurocode 7 for the second generation of Eurocode; Proceedings of the XVI ECSMGE; Edinburg

[3] Bond A.; (2019); Tomorrow's geotechnical toolbox: EN 1990:202x Basis of structural and geotechnical design; Proceedings of the XVII ECSMGE; Reykjavik

[4] GEO5; (2023); Manual; Prague

[5] Maksimović M.; (1996); A Family of Nonlinear Failure Envelopes for Non-Cemented Soils and Rock Discontinuities; Electronic Journal for Geotechnical Engineering; http:geotech.civen.okstate.edu/ejge/ppr9607

[6] Maksimović M.; (2008a); Soil mechanics; Fourth edition; AGM knjiga; Belgrade (in Serbian)

[7] Maksimović M.; (2008b); NENVE-X Freeware – Non-linear soil & rock failure envelopes for PC; Belgrade

[8] Srbakoski M.; (2024); Application of linear and non-linear soil failure envelopes for designing retaining walls; Master thesis; Faculty of civil engineering; Skopje (in Macedonian)

Marko Gjorgjioski
MSc, Civil Engineer
North Macedonia
markogorgioski@hotmail.com

Toni Arangjelovski
PhD, Full Professor
Ss. Cyril and Methodius University in Skopje
Faculty of Civil Engineering – Skopje
0000-0001-6290-5970

Emilija Fidancevski
PhD, Full Professor
Ss. Cyril and Methodius University in Skopje
Faculty of Technology and Metallurgy – Skopje
0000-0003-2919-5916

Goran Markovski
PhD, Full Professor
Ss. Cyril and Methodius University in Skopje
Faculty of Civil Engineering – Skopje
0000-0003-3812-2890

ANALYSIS OF THE INFLUENCE OF MINERAL ADDITIONS ON THE PROPERTIES OF SELF-HEALING CONCRETE

DOI: doi.org/10.55302/SJCE2514153gj

The sustainability of buildings represents one of the biggest problems in the civil engineering industry from the point of view of global economy and ecology. The construction of structures requires a lot of energy and non-renewable resources that generate large amounts of CO_2 during their production, as well as high costs for the construction process itself. Annually, 2.5 tons of concrete are produced per person, and it is known that the main component in concrete is Portland cement. The process of obtaining the cement clinker results in the release of 1 ton of CO_2 for every ton of clinker produced if the calcination emissions and the fuel required for the rotary kiln are taken into account. Taking into account the fact that in 2022 $4.1x10^9$ tons of cement were produced and the CO_2 emissions from that cement were about $3x10^9$ tons, which is assumed to be 5 - 7% of the total CO_2 emissions.

The current solution to this problem is to design structures with a longer lifespan, which is often overestimated due to the lack of maintenance of the structures, which leads to a shorter lifespan of the structures, and which ultimately leads to the need for new structures and thus new input energy and resource. The reason for this accelerated degradation of the structures is the biggest "enemy" of concrete, namely the cracks that are an inevitable part of it. The problem with cracks is that they represent a "shortcut" for aggressive agents that penetrates in the concrete and lead to the corrosion of the reinforcement, thus reducing the load-bearing capacity of the structure.

In such cases, the ability of concrete to heal its own cracks represents a huge opportunity in the field of sustainability of structures, meaning that the structure made of such concrete has an increased lifespan and increased sustainability of the structure. It is for these reasons that in this paper the possibility of self-healing of different concrete mixes will be experimentally investigated and their self-healing efficiency will be determined by monitoring different key parameters and conducting several tests.

Keywords: self-healing; concrete; cracks; durability

1. INTRODUCTION

Reinforced concrete structures often suffer from the problem of cracking, which leads to earlier degradation of properties than that predicted by the design life of the structure. The current practice responds to this problem by designing structures with a much higher quality, which means a higher initial cost of the structure. In addition to higher quality, an extensive and complex program for inspection and maintenance of the structures is also required, which is often very difficult and expensive due to the inaccessibility of some of the structures.

It is precisely for this kind of problem that it is necessary to develop a technology that can detect damage to the structure itself and at the same time repair that damage itself. If we are talking specifically about reinforced concrete structures, there is a possibility of applying technology that can detect the appearance of cracks in the concrete itself and heal them. Incorporating such technology into reinforced concrete raises the material to the level of smart materials.

2. DEFINITION OF SELF-HEALING

The field of self-healing is being researched my multiple world-renowned institutions, each with its own set of definitions for self-healing itself. In this paper the definitions were adopted from The International Union of Laboratories and Experts in Construction Materials, Systems and Structures “RILEM”.

Self-healing is a process that occurs in a material that results in its properties returning to a certain level and thereby improving the material's performance after they have been reduced by a previous action.

Autogenous self-healing is defined when the self-healing process is performed with components of the mixture that would otherwise be present in the material but not specifically intended for self-healing.

Autonomous self-healing is defined when the self-healing process is performed with components of the mixture that would not otherwise be present in the material, i.e., they are added specifically intended for the self-healing process.

Crack sealing is when the properties that affect durability or improve weather resistance (such as permeability) are restored.

Crack healing is when the properties that affect the strength properties are restored, i.e. they improve resistance to mechanical influences (mechanical properties).

3. MECHANISMS OF AUTOGENIOUS SELF-HEALING

As a result of theoretical approaches and experimental procedures, it was concluded that autogenous self-healing is the result of a complex interplay of physical, chemical and mechanical mechanisms within the cement matrix shown in Figure 1. In practice, it is difficult to achieve crack healing with only one of these mechanisms, but it is often possible to observe which of them is the dominant mechanism and what this is due to.

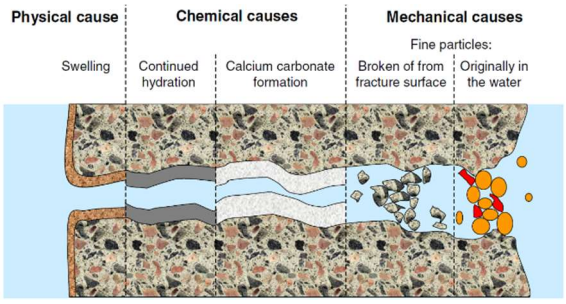

Figure 1. Mechanisms of autogenous self-healing.

The mechanisms can be separated in three groups: physical, chemical and mechanical.

The most dominant physical mechanism is swelling of concrete when the crack surfaces is in contact with the water, it should be noted that this mechanism is theoretically reversable.

There are two dominant chemical mechanisms: continued hydration and formation of $CaCO_3$. When the crack surfaces are in contact with the water, the un-hydrated cement particles start the hydration process and produce C-S-H gel that has bigger volume than the cement particles and seals the crack. Calcium carbonate ($CaCO_3$) forms when calcium hydroxide ($Ca(OH)_2$) which is a product from hydration, reacts with carbon dioxide (CO_2) in the presence of water (H_2O), so the calcium carbonate particles than latch onto the walls of the crack.

The mechanical mechanism represents a blockage of the crack with particles from the crack walls or from the water. This type of healing is unpredictable and is reversible.

4. EXPERIMENTAL REASERCH OF SELF-HEALING CONCRETE

4.1 MIX DESINGS

For the purposes of this experiment, a total of three concrete mix designs were made, all three of which were made with CEM I 52.5R. The first sample was with only cement as a binder, without materials that replace cement, i.e. sample R1. In the second sample 16% of the cement was replaced with mechanically activated fly ash, i.e. sample R1LP16HK1, while in the third sample 10% of the cement was replaced with finely ground dolomite, i.e. sample R1D10HK1. The corresponding mix designs are given in Table 1.

Table 1. Mix design of samples with CEM I 52.5R

Mix design	CEM I 52.5R	Water	Aggregate	Fly ash	Dolomite	Hidrofob Kristal	PP Fiber	Super-plasticizer
R1	360 kg	200 kg	1840 kg	/	/	/	12 kg	5.40 l
R1LP16HK1	302.40 kg	200 kg	1840 kg	57.60 kg	/	3.60 kg	12 kg	5.40 l
R1D10HK1	324 kg	200 kg	1840 kg	/	36 kg	3.60 kg	12 kg	5.40 l

All samples have a superplasticizer with a dosage of 1.5% in relation to cement in order to increase the workability of the concrete. Due to the need to open a crack and keep the crack opening stable in all samples, without causing failure of the concrete samples, polypropylene (PP) fibers with a length of 50 mm were added with a dosage of 0.5% in relation to the weight of the concrete. A water-cement factor of 0.55 was maintained in all mix designs. To increase the efficiency of self-healing in all samples except in the standard sample R1 a crystal-forming additive Hidrofob Kristal (ADING) was added with a dosage of 1% in relation to cement. In order to maintain the same amount of Hidrofob Kristal and superplasticizer, the initial amount of cement, i.e. 360 kg, was always taken when calculating the dosage. Each sample consists of twelve test specimens, namely nine prisms with dimensions 10/10/40 cm and three cubes with sides of 15 cm.

Figure 2. Test examples.

4.2 EXPERIMENT COURSE

After casting the specimens according to the mix design, ultrasonic pulse velocity (UPV) was measured longitudinally and transversely of the specimen at age of 7 and 28 days. At age of 28 days the mechanical i.e. compressive strength and bending strength of the concrete were determined in accordance with the standards MKC EN 12390-3:2019 and MKC EN 14651+A1:2010 respectively.

After 28 days of age a crack was created in six of nine specimens, the UPV was measured again to see the effect of the crack and also the crack width was measured with digital microscope camera. After that three of the cracked specimens were fully submerged in water to promote self-healing. During this period at 2, 7 and 28 days after submerging the crack width was measured in the same places as before. After 28 days of treatment the specimens were removed from the water and are dried for 7 days to a constant weight, then the UPS was measured to determine the effect of the self-healing.

Following these, all nine specimens were coated with epoxy resin except a surface of 10x5 cm on the bottom of the specimen and the specimens were submerged in water for a depth of 2 ± 0.5 cm to achieve capillary water absorption according to standard MKC EN 13057:2009. The weight of the capillary absorbed water was controlled after 15 min, 30 min, 1h, 2h, 4h, 8h and 24h. This data was used to determine the efficiency of self-healing.

4.3 METHODS OF DETERMINING THE EFFICIENCY OF SELF-HEALING

One of the main challenges in the field of self-healing concrete is the lack of standardization, which hinders the advancement of research to a higher level. This has resulted in a variety of experimental approaches and the use of different self-healing indices to quantify healing efficiency, often leading to inconsistent results and conclusions in literature. The general approach adopted by researchers involves testing a physical or mechanical property of the concrete before and after crack healing. By comparing these stages—the premises are expressed as a percentage or self-healing index—the healing efficiency is determined. In the following only those relevant to this paper will be presented.

When self-healing is monitored via optical microscopy, crack width can be measured from processed images. The healing efficiency is

quantified using the Crack Closure Index (ICS), defined as:

$$ICS = \frac{w_{pre-healing} - w_{post-healing}}{w_{pre-healing}} \quad (1)$$

where $w_{pre-healing}$ is the crack width before treatment, and $w_{post-healing}$ is the crack width after treatment.

Similarly, the Self-Healing Index (ISH) can be applied when healing efficiency is evaluated through a capillary absorption test. In this case, the parameter of interest is the amount of water absorbed through specimens with unhealed cracks and specimens with healed cracks. The index is then calculated as:

$$ISH_{sorptivity} = \frac{S_{crack,unhealed} - S_{crack,heale}}{S_{crack,unhealed}} \quad (2)$$

where $S_{cracked}$ is the sorption coefficient of unhealed specimens and S_{healed} corresponds to healed specimens.

5. TEST RESULTS

5.1 MECHANICAL PROPERTIES

5.1.1 Compressive strength

Compressive strength was tested on cubes with a side of 15 cm, according to the standard MKC EN 12390-3:2019 at an age of 28 days, as shown in Figure 3.

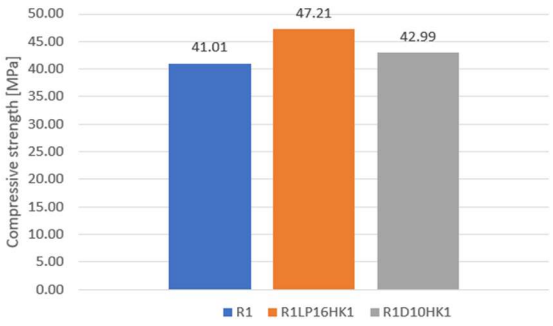

Figure 3. Compressive strength of specimens.

The results show that the sample with mechanically activated fly ash has the highest compressive strength, as the finer particle size increases reactivity compared to ordinary fly ash. The strengths of the cement-only sample and the one with dolomite are similar. It is also evident that the crystal-forming additive does not reduce compressive strength, which is an important property.

5.1.2 Bending strength

The bending strength was tested on prisms with dimensions of 10/10/40 cm, using a three-point flexure test, according to the standard MKC EN 14651+A1:2010 at an age of 28 days. The results are shown on Figure 4.

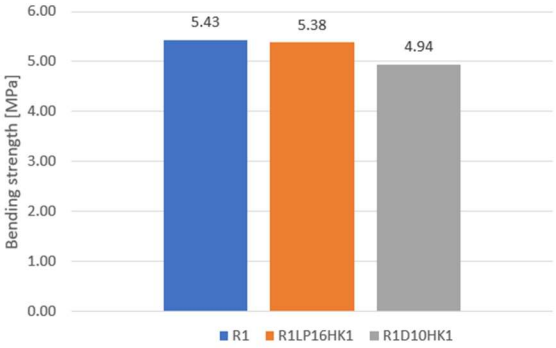

Figure 4. Bending strength of specimen.

The results show that the sample with only cement and the one with fly ash have the same flexural tensile strength, while the sample with dolomite shows slightly lower values but still within the same range, indicating that the type of additive does not significantly affect flexural tensile strength.

5.2 ULTRASONIC PULSE VELOCITY

A total of 531 measurements were carried out on nine prisms and three cubes from three concrete mix designs. Only the characteristic results relevant for drawing conclusions are presented below. The UPV for the specimens in three states: 28 days age before crack, 28 days age after crack and after 28 days treatment as shown in Figure 5.

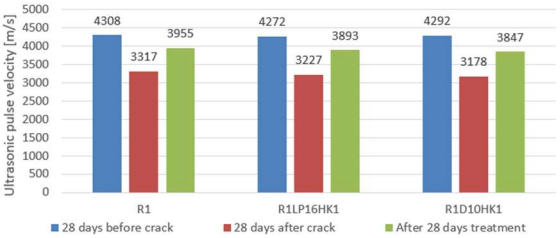

Figure 5. UPV in three states measured longitudinally.

The same results can be shown on a graph for a better representation as shown in Figure 6.

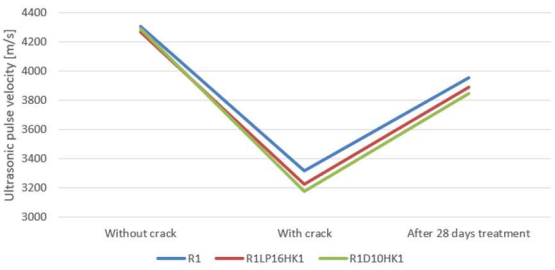

Figure 6. UPV in three states measured longitudinally.

From the results, it can be concluded that there is a clear trend of decreasing direct wave propagation velocities after the appearance of a crack, followed by a partial recovery to the range of reference values (before cracking) after 28 days of treatment.

In the next graph as shown in Figure 7, a correlation is made between the measured crack width with ultrasonic pulse velocity, before and after treatment of the specimens. The data for the crack width is taken from Figure 8.

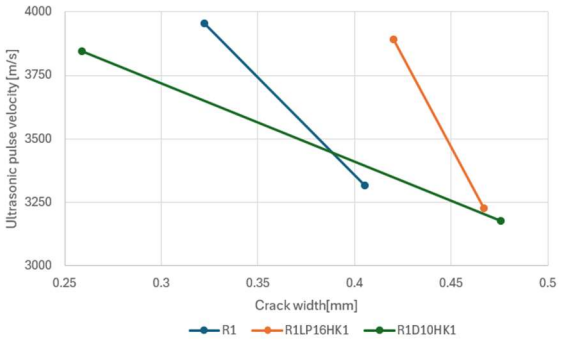

Figure 7. Correlation of UPV in longitudinal direction with the crack width before and after treatment.

The presented results clearly show the correlation between crack width and ultrasonic pulse velocity through the specimen, as the crack width decreases due to self-healing, the ultrasonic velocity increases.

5.3 MICROSCOPIC MONITORING

The self-healing process was also monitored on the surface with a microscope camera at six measurement points on three sides of the prism.

In Figure 8 the average healed and unhealed crack width is shown. The crack width is measured on three prisms that were under treatment, before and after the treatment on the bottom side of the prism in two points (K5 and K6).

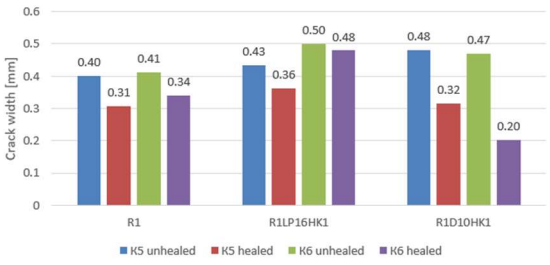

Figure 8. Measured crack width before and after treatment.

The graph shows the self-healing of the crack in every mix design and on both measuring points, but due to the localized effect of crack sealing this type of data cannot be used to determine the efficiency of the self-healing.

5.4 CAPILLARY ABSORPTION

Three uncracked specimens, three specimens with an unhealed crack, and three specimens with a healed crack were coated with two layers of epoxy on the entire bottom surface and up to half of the side surfaces, leaving an uncoated area of 5 × 10 cm on the bottom side. This uncoated part was designated for water absorption and where the crack is located.

The procedure for testing capillary water absorption followed the standard MKC EN 13057:2009 ,with slight modifications regarding specimen geometry and immersion depth. All prisms were placed inside a closed container of water on spacers, so that there was a gap between them and the bottom of the container, allowing free circulation of water. The immersion depth was 2.0 ± 0.5 cm. At intervals of 15 minutes, 30 minutes, 1 hour, 2 hours, 4 hours, 8 hours, and 24 hours, the masses of the prisms were measured, and the amount of absorbed water was calculated over time.

Water uptake per unit area (kg/m^2) was calculated as:

$$i = \frac{W}{A} \tag{3}$$

where W is the absorbed water (kg) over a given time interval and A is the exposed surface area (m²).

The sorption coefficient (S) was determined as the slope of the linear relationship between i (kg/m^2) and the square root of immersion time ($h^{0.5}$). One of the graphs is shown on Figure 9.

Self-healing efficiency (*SE*, %) was quantified by comparing cracked–unhealed and cracked–healed sorption coefficients, using:

$$SE = \frac{S_{crack,unhealed} - S_{crack,heale}}{S_{crack,unhealed}} \tag{4}$$

where $S_{cracked}$ is the sorption coefficient of unhealed specimens and S_{healed} corresponds to healed specimens.

With such measurements, the entire self-healing process can be quantified, allowing a clearer evaluation of the effect of different mineral additives on self-healing, as well as the possibility to compare them with each other.

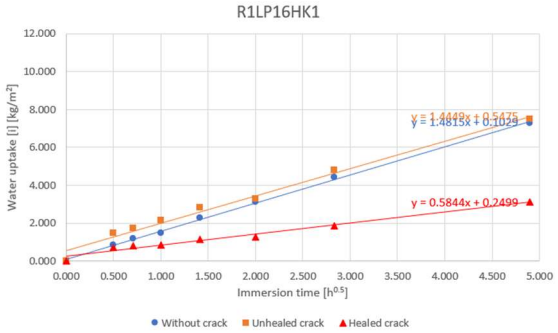

Figure 9. Capillary absorption of samples from R1LP16HK1 mix design.

Based on this and all other graphs, summary results are shown on Figure 10 for all mix designs.

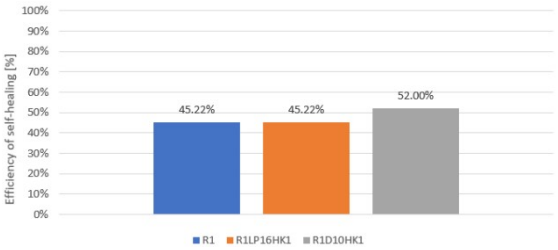

Figure 10. Summary results on self-healing efficiency.

The results indicate that self-healing also occurred in mix design R1 without mineral additions or crystalline admixtures. For mix design R1LP16HK1, the same level of self-healing efficiency as in R1 was observed, due to the short treatment period of 28 days. For mix design R1D10HK1, the highest self-healing efficiency was observed after 28 days of treatment.

6. SUMMARY

This study evaluated the influence of mineral additions (fly ash, dolomite) and a crystalline admixture on the mechanical behaviour, ultrasonic pulse velocity, and self-healing efficiency of concrete. The results showed that mineral additions and the crystalline admixture had little effect on flexural tensile strength, while the highest compressive strength was achieved in the mix with fly ash (R1LP16HK1) due to its increased reactivity, followed by R1 and R1D10HK1, the latter influenced by the expansive behaviour of MgO from dolomite hydration. The crystalline admixture itself had no significant effect on mechanical properties.

Ultrasonic testing confirmed the presence of self-healing, with an initial decrease in velocity after cracking and a subsequent recovery after 28 days of water treatment, consistent with crack filling.

Microscopic monitoring revealed localized deposition of healing products. However, capillary absorption testing quantified healing efficiency: the highest value (52.0%) was recorded for the dolomite mix (R1D10HK1), due to the high calcium ion availability from CaO and the effect of the crystalline admixture. The reference mix (R1) also showed considerable efficiency (45.2%), attributed to un-hydrated cement and calcium hydroxide, while the fly ash mix (R1LP16HK1) showed comparable, though slower developing, healing due to the delayed pozzolanic reaction.

Overall, the results demonstrate that self-healing occurs in all mixes, with efficiency depending on the type of mineral additive and available calcium sources. Longer curing periods are recommended to better assess the continued effect of fly ash and crystalline additives over time.

ACKNOWLEDGEMENT

The first author would like personally to express his gratitude for the opportunity to participate in the project “Sustainable Partnership for Innovations Based on Application of Circular and Nano Materials in the Process Industry” submitted by the leading partner Ss. Cyril and Methodius University in Skopje, Faculty of Civil Engineering Skopje, financed by Ministry of Economy, No.18-4427/3 from December 2023-October 2024 under which these types of concrete were developed.

REFERENCES

[1] M. De Rooij, K. Van Tittelboom, N. De Belie, E. Schlangen, (2013) “Self-Healing Phenomena in Cement-Based Materials”, RILEM State Art Reports, Vol. 11.

[2] I. Stefanovska, E. Fidanchevski, (2023), “Self-healing of cement mortars based on fly ash and crystalline admixture”, MATEC Web of Conferences, Vol. 378, SMARTINCS’23, Ghent, Belgium, article number 02018.

[3] K. Van Tittelboom, E. Gruyaert, H. Rahier, N. De Belie, (2012) “Influence of mix composition on the extent of autogenous crack healing by continued hydration or calcium carbonate formation”, Construction and Building Materials Vol. 37, pp. 349–359.

[4] L. Ferrara, (2017) “An overview on the research on self-healing concrete at Politecnico di Milano”, MATEC Web of Conferences, Vol. 120, 02001.